Molecular dynamics simulations of Krytox^{TM} oil - CO_2 gas mixture

Computation of transport and thermodynamic properties

Kunal Harshad Mavani

Master of Science Thesis

TU Delft Delft University of Technology

Energy and Process Technology

Molecular dynamics simulations of Krytox^{TM} oil - CO_2 gas mixture

Computation of transport and thermodynamic properties

by

Kunal Harshad Mavani
Student number: 5010012

in partial fulfillment of the requirements for the degree of

Master of Science
in Mechanical Engineering

at the Delft University of Technology,
to be defended publicly on Monday July 5, 2021 at 09:00 AM.

Supervisors:	Dr. Othon Moultos
	Dr. Hanieh Bazyar
Daily supervisor:	Dr. Alper Celebi
Committee:	Prof. Dr. Ir. Thijs Vlugt
	Dr. Ir. Mahinder Ramdin
	Dr. Poulumi Dey

Faculty of Mechanical, Maritime and Materials Engineering (3mE) · Delft University of Technology

"Don't tell people how to do things, tell them what to do and let them surprise you with their results."

George S. Patton

Acknowledgements

On 20th October 2020, I started with my thesis in the field of molecular simulations. Curious to explore a new field of study and fascinated to work on a supercomputer were the prime movers for me to take up this project. I have come a long way both technically and as a person in the past nine months with the contribution of many people.

I would first like to thank my supervisor Dr Othon Moultos for his guidance throughout the project. The meetings we had were technically insightful. I always felt motivated and charged up after the meetings. I would next like to thank Dr Alper Celebi, my daily supervisor during the initial phase of the thesis, for providing me with a head start in getting acquainted with LAMMPS and the cluster environment. I am thankful to Dr Hanieh Bazyar for providing me with the experimental data for validation of my results and quick response to my queries both over emails and virtual meetings.

I am grateful to Dr Agilio Padua and Dr Axel Kohlmeyer from the LAMMPS community who have been very active in responding to my queries about various commands and functions in LAMMPS. I would also like to thank Mr Fabian Grunewald from the University of Groningen for helping me with the implementation of the MARTINI force field for Krytox^{TM} oil. I am also thankful to Mr Gerben Roest for the IT support without which it would not have been possible to run simulations efficiently.

Next, I would like to thank my younger brother Harsh Mavani for getting me acquainted with the Linux environment and assisting me with troubleshooting issues. I am grateful to my friends in Delft and also my friends from high school and bachelor's education who have been with me throughout this journey. My deepest gratitude to my parents for their support and encouragement in all my decisions. During this journey, my relationship with them has grown stronger.

Kunal Harshad Mavani
June 25, 2021

Abstract

The power plant, steel and petrochemical industries are large sources of carbon emissions worldwide. For meeting the climate goals of 2030 and 2050, efforts are underway towards pioneering novel technologies. Gas separation by supported liquid membranes is an attractive option for its energy-efficient, continuous and low cost of operation. The separation of gases takes via a solution diffusion mechanism where the gases are separated based on their selectivity. Krytox^{TM} oil is a high performance perfluoropolyether polymeric lubricant, originally aimed for its application to supersonic transport aircraft. The lubricant is known for its chemical and thermal stability leading to a longer usable life. The oil has shown an affinity for carbon dioxide (CO_2) gas, a weak Lewis acid, owing to the fluorine and oxygen atoms in the polymeric oil which act as Lewis base and is thus envisioned for use in supported liquid membranes for gas separation.

Molecular dynamics simulations serve as a powerful tool of study, overcoming the shortcomings of experimental methods such as the difficulty of measurements at elevated temperatures, pressures or handling dangerous chemicals. This project covers the study of transport properties of Krytox^{TM} oil namely the oil viscosity and diffusivity of CO_2 in the oil for varying conditions of temperature, pressure and polymer chain length using equilibrium molecular dynamics simulations. The suitability of various atomistic force field models for this particular study has been tested, proceeding with the Universal force field (UFF) as the model of choice for studying the oil properties. To shorten the simulation time and study long time scales, coarse-grained simulations have been carried out using state-of-the-art MARTINI force field. In addition to transport properties, Henry's constant for the solubility of CO_2 in Krytox^{TM} oil has been predicted via alchemical free energy calculations by molecular dynamics simulations.

Table of Contents

Chapter 1

Introduction

The increase in the emissions of carbon dioxide (CO_2) is leading to global warming and worsening climatic conditions and has become a pressing issue for the last few decades [1]. A well-matured technology for absorbing CO_2 using amine is widely used but faces shortcomings for its energy inefficiency and also for corrosive, degradation sensitive and high volatile nature of amines [2]. Membrane gas separation is an important part of various industrial processes and can be implemented for CO_2 capture, for instance from flue gas. Supported liquid membranes (SLM) are considered one of the most efficient membrane separation processes with ease of scalability. In SLM, an organic liquid is embedded in pores and sustained thereby capillary forces [3]. The separation takes place via solution-diffusion model, in which the diffusion coefficient is about three-four times higher than in polymer membranes [4]. For this purpose, research has been carried out for SLM using ionic liquids. Ionic liquids have shown higher selectivity for CO_2 in comparison to other gases such as N_2, H_2, CH_4 [4]. Fluorination of ionic liquids has shown an increased solubility of CO_2 gas, a weak Lewis acid, owing to electronegative nature of fluorine [5], for which solubility data is reported in the literature [6][7][8]. Ionic liquids have attracted attention because of their nonvolatile, nonflammable and nonexplosive nature [9]. But because of its high cost, high viscosity and environmental issues, ionic liquids have not yet been successfully commercially implemented [2][7]. Some of the biological impacts of ionic liquids include cytotoxicity and resistance to biodegradation [9].

Krytox^{TM} oil, a fluorinated polymeric ether is a high-grade lubricant developed by DuPont initially for the aerospace industry [10]. Experimental research at the Process and Energy department, TU Delft has shown that this fluorinated ether has potential for CO_2 absorption. This project is dedicated mainly to studying the transport properties of Krytox^{TM} oil using molecular dynamics (MD) simulation for its potential use as a solvent for CO_2 absorption. The work can further elucidate the potential application of Krytox^{TM} oil as a solvent in SLM for gas separation applications focusing on CO_2 removal.

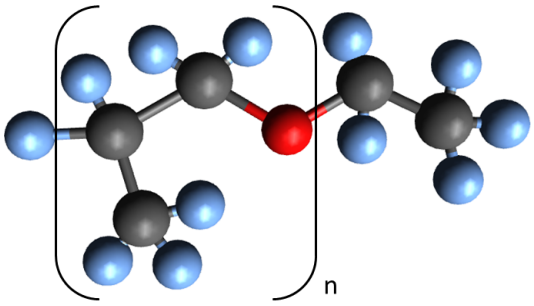

Figure 1-1: Chemical structure of Krytox™ oil. Oxygen atom is red, carbon atoms are black, fluorine atoms are blue. The part in between the brackets represent one monomer (figure produced using Avogadro software [12]).

1-1 Krytox™ oil characteristics

Krytox™ oil is a trademark oil from DuPont used for lubrication purposes. The oil is a clear, colourless perfluoropolyether [11]. The chemical structure of oil, F-($CF(CF_3)$-CF_2-O)$_n$-CF_2-CF_3, consists of three types of atoms: carbon, fluorine and oxygen, shown in figure 1-1 with polymeric chain length varying in the range n = 4-60. A polymeric oil is a mixture of molecules of various chain lengths. Based on the average value of molecular weight which determines the average value for the number of monomers in a molecule, a particular grade of oil is defined as highlighted in table 1-1. As per the product catalogue [11], the oil density and viscosity vary based on the chain length and operating conditions.

Table 1-1: Average molecular weight and corresponding number of monomers for Krytox® 100 series of perfluoropolyethers [13].

Krytox® GPL	**Average molecular weight ($g\,mol^{-1}$)**	n_{avg}
100	960	4.95
101	1180	6.28
102	1720	9.53
103	2275	12.8
104	3150	18.1
105	4730	27.7
106	5490	35.0
107	7475	44.2

Krytox™ oil is used as a lubricant for industrial and automotive bearings. It is suitable for high-temperature applications up to a temperature of 200 °C. Because of its low vapour pressure, it is also suitable for vacuum applications. The cost-effective Krytox™ oil has several advantages justifying its use as a robust lubricant [10]:

- Chemical, biological and environmental inertness.
- Non-hazardous to the atmosphere or ozone layer
- Longer usable life

1-2 Motivation

For a long time now macroscopic property study of fluids is done experimentally. Not undermining the importance of property determination through experiments and its necessity, experimental methods might face some shortcomings. Experimental measurements are costly and may turn out difficult to perform under extreme temperature and pressure conditions [14]. Considering the above drawbacks along with the increase in the computational power of the new generation computers, molecular simulations have gained importance and has become an integral part of research in various field of sciences [15]. It is a powerful tool for computing the thermodynamic and transport properties of pure fluids and mixtures thus complementing the experimental results.

Section 1-1 listed various points that substantiate the use of Krytox^{TM} oil for lubrication purposes. This project considers putting the oil to alternate use for gas separation and carbon capture. Experiments have shown an increase in the CO_2 solubility in ionic liquids by substituting the alkyl chain in a hydrocarbon by fluoroalkyl chain [6]. The similarity of low polarizability/dipolarity parameters of both CO_2 and perfluorinated compounds leads to stabilization of charge or dipole by solvent and is attributed for the high solubility of CO_2 in fluorinated compounds. The electron-donating capacity of oxygen in polyfluoroethers enhances the solubility of CO_2 which is a weak Lewis acid [5]. The ab initio calculations performed by Raveendran et al. [16] suggest the interaction between the carbon atom of CO_2 acting as a weak Lewis acid with the fluorine atoms of polyfluoroether acting as weak Lewis base for the higher solubility of CO_2. The same study also suggests that the oxygen atoms in CO_2 act as weak Lewis base and interacts with the hydrogen atom of the fluorinated hydrocarbon. Thus, an optimum degree of fluorination increases the solubility of CO_2 in the oil.

This research project is mainly concerned with the study of transport properties namely CO_2 in diffusivity Krytox^{TM} oil and viscosity of the oil. The solubility of CO_2 in Krytox^{TM} oil though important is not the primary motive as it involves separate Monte Carlo (MC) simulations (although prediction of Henry's constant by alchemical free energy calculations using MD simulations has been carried out in chapter 6). The ulterior motive is to use Krytox^{TM} oil for SLM. Viscosity tabulation is important as it affects the diffusion [17] of gases through the liquid membrane and also affects the pumping cost in process industries. For mass transfer through a dense membrane, the flux rate is controlled by the permeability of the membrane [18]. Permeability (P_i) is a function of the solubility (given by Henry's constant (K_{H_i})) and diffusion coefficient (D_i) as shown in equation 1-1.

$$N_i = \frac{K_{H_i} D_i}{l} \left(p_{i_F} - p_{i_P}\right) = \frac{P_i}{l} \left(p_{i_F} - p_{i_P}\right) \tag{1-1}$$

where:

N_i = Molar transmembrane flux of species i
K_{H_i} = Henry's constant for species i
D_i = Diffusion coefficient of species i
l = Membrane thickness
p_{i_F} = Partial pressure of species i on the feed side
p_{i_P} = Partial pressure of species i on the permeate side
P_i = Permeability of species i

The process of membrane separation is depicted in figure 1-2. From the above discussion, it is concluded that the study of the diffusion coefficient of CO_2 in the oil is of importance for predicting the mass transfer coefficient. Robustness of Krytox^{TM} oil for its use as a lubricant

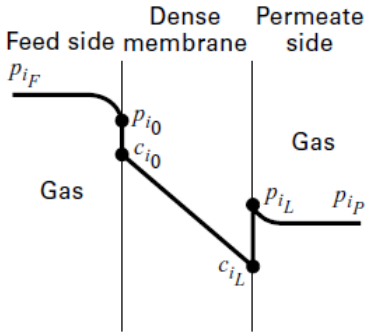

Figure 1-2: Gas separation using SLM [18].

along with its affinity for CO_2 serves as a stimulus for academic and industrial research in the field of gas separation using MD simulations.

1-3 Literature review

Recently some work in the field of MD simulations has been carried out related to perfluorinated compounds. This section summarizes the relevant research done so far and its usefulness to this project.

Li et al. [19] have developed a force field model for molecular simulation of perfluoromethylpropyl ether. A united atom model is proposed and is shown to accurately reproduce the phase equilibrium data. The model has not been tested for bulk transport properties. The literature mentions that intramolecular interactions are important for predicting the transport properties and thus the model is not expected to provide correct predictions for transport properties.

McCabe et al. [20] compared the transport properties using both united atom (by Cui et al. [21]) and explicit atom (by Borodin et al. [22]) schemes. The compounds taken into consideration were short perfluoroalkanes mainly perfluorobutane, perfluoropentane, perfluorohexane, and perfluoroheptane. Viscosity was estimated using both equilibrium molecular dynamic simulation (EMD) and non-equilibrium molecular dynamic simulation (NEMD). The

self-diffusivity of compounds was estimated using EMD. The united atom model developed by Cui et al. is suitable only for predicting vapour-liquid phase equilibrium properties. Viscosity determined using this model was under-determined whereas self-diffusivity was overpredicted as compared to experimental results. The explicit atom model by Borodin et al. is a quantum chemistry based force field. Viscosity and diffusivity measured using this explicit atom force field model were representatives of the experimental results. A point of note is that neither of the models takes into account the partial charges (coulombic) leading to computationally efficient simulations. The explicit force field model was not used for this project for the non-availability of force field parameters for the oxygen atom in the literature.

Koike [23] has studied the tribological behaviour of branched and linear perfluoropolyethers using the consistent valence force field (CVFF). As a part of the research, viscosity as a function of shear rate was determined for Krytox^{TM} molecule with the number of monomers $n = 4, 9$. The results agreed well with the available experimental data. CVFF was explored as a potential force field option for this project.

Along the similar lines of Koike, Jiang et al. [24] have estimated the rheological properties of perfluoropolyether $C_8F_{18}O_4$ through MD simulation using the Universal force field (UFF). Contribution by electric charges was not considered claiming that the effect is taken into account by the other potential parameters. This could prove to be an advantage as leaving out electric charges results in a reduction of computation cost. The authors have tabulated viscosity as a function of shear rate. Viscosity was calculated across a wide range of shear rate with many data points making it possible to predict zero shear viscosity. UFF has been explored to a greater depth for this project for predicting the transport properties using EMD simulations.

In very recent research, Black et al. [25] have developed an all-atom (AA) force field for molecular simulations of perfluoropolyethers. The force field has been tested for validating the heat of vaporization and liquid densities of perfluorodiglyme (CF_3-O-(CF_2-CF_2-O)$_2$-CF_3) and perfluorotriglyme (CF_3-O-(CF_2-CF_2-O)$_3$-CF_3). The force-field was developed by considering OPLS-AA originally developed by Jongersen et al. [26] as the base case. The bonded parameters for the potential were modified based on the ab initio quantum mechanical calculations to replicate the molecular structure. The Lennard-Jones potential parameters were adjusted to replicate the experimental density and heat of vaporization. Electric charges for coulombic potential were taken from the native OPLS-AA force field to ensure the transferability of parameters. This modified OPLS-AA was considered as an alternative for this project.

The right choice of the force field for transport properties prediction was made after extensively performing simulations using the force field models implemented by Koike [23], Jiang et al. [24] and Black et al. [25].

1-4 Research objective and scope

This section describes the goal of the thesis and the path that was followed to meet the objectives. As described briefly in section 1-2, the main objective of the thesis is to estimate the

transport properties of Krytox^{TM} oil and its mixture with CO_2. From the literature review (refer section 1-3) it was observed that extensive research regarding tabulation of transport properties for different variants of Krytox^{TM} oil (varying chain length) is not carried out.

Thus, computation of transport properties was carried out which included estimating the diffusivity of CO_2 in the Krytox^{TM} oil and viscosity of the oil. Thermodynamic property, mainly the density was computed. Also, the structure of the oil molecule was studied by computing the radius of gyration and end-to-end distance. The interaction of oil with CO_2 was studied by calculating the radial distribution function (RDF). The above-mentioned properties were computed for varying chain length of Krytox^{TM} oil for different operating conditions of temperature and pressure. All the MD simulations were performed using the EMD simulation method in Large-scale Atomic/Molecular Massively Parallel Simulator (LAMMPS) [27], an open-source platform. Transport properties were computed in LAMMPS using an in-house developed on-the-fly computation of transport properties (OCTP) tool by Jamali et al. [28]. Methodology, simulation procedure and discussion of results for atomistic simulations are covered in chapters 2, 3 and 4 respectively.

Simulations using the traditional atomistic force field models are computationally intensive and time-consuming especially for long-chain polymers consisting of many atoms. Thus, an effort was made towards coarse-graining the polymer molecule using MARTINI 3 force field [29] which consists of X-class beads for halo-compounds. For the coarse-grained Krytox^{TM} oil molecule, the simulations were performed in GROMACS [30]. Simulation details and results are discussed in chapter 5.

The study of the solubility of CO_2 in the oil is not one of the major objectives of the project. But it is an important parameter for determining the molar flux of solute through a dense membrane (equation 1-1). Thus, computation of Henry's constant for solubility of CO_2 in Krytox^{TM} GPL 101 was performed by alchemical free energy calculations [31][32] using MD simulations in LAMMPS. Simulation details and results are discussed in chapter 6.

Chapter 2

Computation of transport properties and selection of force field

This chapter briefly describes the general procedure of MD simulation in section 2-1. The details are available in the sources elsewhere [14][33]. Transport properties calculation by Einstein relation using OCTP tool in LAMMPS is described in section 2-2. At the heart of an MD simulation, are the force field parameters utilized for integrating Newton's equations of motion. Selection of force field parameters is crucial, the discussion for which is carried out in section 2-3.

2-1 Molecular dynamics simulation methodology

The choice of the type of molecular simulations method for this research was MD simulations as transport property tabulation is not directly possible using MC simulations because of its non-deterministic nature. MD simulation can be classified into EMD simulation and NEMD simulation. For this particular project, the EMD simulation method was used for transport properties prediction. The details are covered in section 2-2.

MD simulations follow a similar procedure as in a physical experiment. System preparation is done by placing atoms/molecules in a simulation box with the initial position and velocity specified. The forces are determined based on the specified force field (potential) parameters (refer section 2-3). The trajectory of each atom is determined by numerically integrating Newton's laws of motion for each timestep of the simulation run. The system temperature and pressure conditions are maintained by implementing a suitable thermostat and barostat. The extensive data of position, velocity and forces obtained for each timestep for each atom is used for computation of various thermodynamic and transport properties [33][34]. The methodology of MD simulation is shown by the flowchart in figure 2-1.

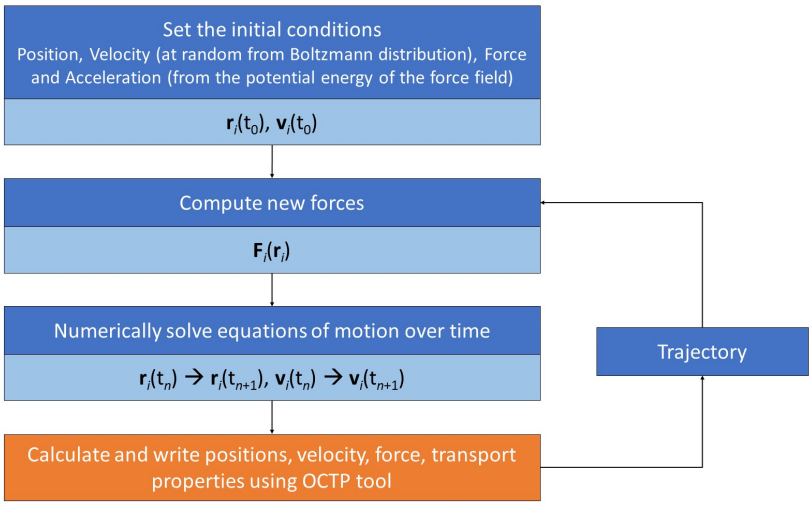

Figure 2-1: MD simulation algorithm for computing properties.

2-2 Computation of transport properties in LAMMPS

The transport properties were calculated using EMD simulations which offers the advantage of obtaining multiple transport properties from a single simulation, unlike NEMD simulations which requires a specific driving force for the computation of the desired property. The transport properties were computed in LAMMPS using the OCTP tool. The OCTP tool uses Einstein relation (equation 2-1) where $(A(t) - A(0))^2$ is the mean-squared displacement (MSD) of the dynamical variable. The ensemble-averaged MSD over a simulation time (t) provides the value of transport property (γ).

$$\gamma = \left\langle (A(t) - A(0))^2 \right\rangle / 2t \tag{2-1}$$

The relevant transport property was computed where the log-log slope for the Einstein relation equalled 1 [14][33] which corresponded to a linear region (with the line passing through the origin). Shown in figure 2-2 is the plot for CO $_2$ diffusivity calculation. The part in the red box known as the diffusive regime is of interest where the log-log slope equal to 1. The part in the blue box is known as the ballistic regime where motion due to inertia dominates. A similar plot can also be obtained for viscosity calculation. Transport properties can also be computed using the Green-Kubo relation [33] which uses a time-correlation function that converges to zero very slowly. The OCTP tool used herein utilizes the order-n algorithm developed by Dubbeldam et al. [35] for storing and processing data thus reducing computational power requirement.

2-2-1 Diffusion coefficient

Diffusion can be intuitively thought of as the distance travelled by a particle in space. The self-diffusion of a species in an isotropic three-dimensional system is given by equation 2-2 for which the MSD is calculated based on the ensemble average. For a simulation inside a

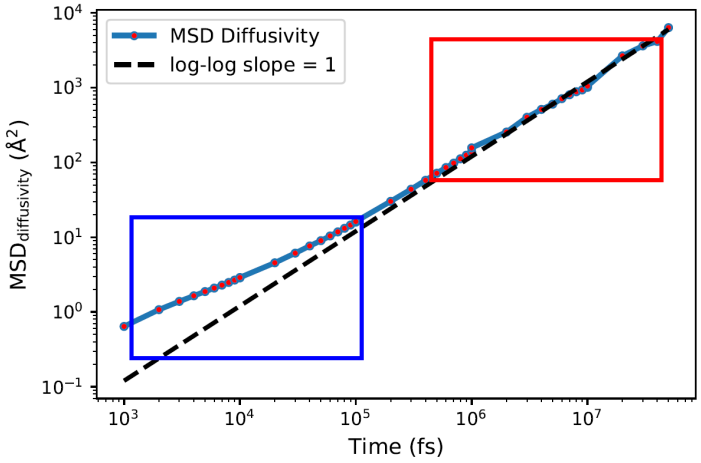

Figure 2-2: MSD plot for computing CO_2 diffusivity in Krytox GPL 102 at 297.15 K temperature and 1 atm pressure using UFF for a simulation run of 50 ns.

box, the effect of a particle crossing a periodic boundary is taken into account in the MSD calculation.

$$D_{i,\text{ self}} = \lim_{t\to\infty} \frac{1}{2t}\frac{1}{3N_i}\left\langle \sum_{j=1}^{N_i} \left(\mathbf{r}_{j,i}(t) - \mathbf{r}_{j,i}(0)\right)^2 \right\rangle \tag{2-2}$$

where:

$D_{i,\text{self}}$ = Ensemble-averaged self-diffusion coefficient of species i
t = Time
N_i = Number of molecules of species i
$\mathbf{r}_{j,i}$ = Position vector of j^{th} molecule of species i

In a binary or multicomponent system especially it is easier to define a system in terms of Maxwell-Stefan (MS) diffusivity which is more general and considers chemical potential as the driving force [36]. In terms of MSD, MS diffusivities are defined in terms of Onsager coefficients (Λ_{ij}). Onsager coefficients are computed from the cross-correlation of the displacement of the molecules of species i and j for the total number of molecules (N) by equation 2-3 [28].

$$\Lambda_{ij} = \lim_{t\to\infty} \frac{1}{2t}\frac{1}{3N}\left\langle \left(\sum_{k=1}^{N_i} \left(\mathbf{r}_{k,i}(t) - \mathbf{r}_{k,i}(0)\right)\right) \cdot \left(\sum_{l=1}^{N_j} \left(\mathbf{r}_{l,j}(t) - \mathbf{r}_{l,j}(0)\right)\right) \right\rangle \tag{2-3}$$

The MS diffusivity (D_{MS}) is then calculated using equation 2-4 [36] based on the mole fraction (x) of species in the mixture.

$$D_{\text{MS}} = \frac{x_2}{x_1}\Lambda_{11} + \frac{x_1}{x_2}\Lambda_{22} - 2\Lambda_{12} \tag{2-4}$$

Fick's diffusivity (D_{Fick}) is defined in terms of the concentration gradient and is related to MS diffusivity by a thermodynamic factor Γ, which is the measure of non-ideality of the mixture [36]. For the dilute system in consideration (CO_2 in Krytox$^{\text{TM}}$ oil), the three diffusivities defined above are equal, shown by equation 2-5.

$$D_{\text{self}} = D_{\text{MS}} = D_{\text{Fick}} \tag{2-5}$$

The diffusivity calculated by MD simulation is affected by the size of the box. Its value is under-predicted as compared to the experimental value. The diffusivity obtained from MD simulation was corrected for hydrodynamics using equation 2-6 where the value of ξ is 2.837298 for cubic lattices [37]. The viscosity (η) used in the equation was obtained from MD simulation and is not affected by system size.

$$D^{\infty}_{\text{Self}} = D^{\text{MD}}_{\text{Self}} + \frac{k_{\text{B}}T\xi}{6\pi\eta L} \tag{2-6}$$

where:

D^{∞}_{Self} = Self-diffusivity corrected for finite-size effects
$D^{\text{MD}}_{\text{Self}}$ = Self-diffusivity computed from MD simulations
k_{B} = Boltzmann constant
T = Temperature
ξ = 2.837298
η = Viscosity from MD simulations
L = Box width

2-2-2 Dynamic viscosity

Using EMD, the viscosity predicted is the zero-shear or Newtonian viscosity. The ensemble-averaged viscosity ($\eta_{\alpha\beta}$) is calculated for the MSD based on the off-diagonal terms of the stress tensor ($P_{\alpha\beta}$) for a specified volume of the simulation box (V) using equation 2-7. For details literature by Mondello et al. [38] should be referred to.

$$\eta_{\alpha\beta} = \lim_{t\to\infty} \frac{1}{2t}\frac{V}{k_{\text{B}}T}\left\langle \left(\int_0^t P_{\alpha\beta}\left(t'\right) \mathrm{d}t' \right)^2 \right\rangle \tag{2-7}$$

In simplistic terms the pressure tensor is computed using equation 2-8 [27].

$$P_{\alpha\beta} = \frac{\sum_k^N m_k v_{k_\alpha} v_{k_\beta}}{V} + \frac{\sum_k^N r_{k_\alpha} f_{k_\beta}}{V} \tag{2-8}$$

where:

m_k = mass of atom k
v_{k_α} = α component of the velocity of atom k
v_{k_β} = β component of the velocity of atom k
r_{k_α} = α component of the distance of atom k from a reference position
f_{k_β} = β component of the force on atom k

An important point to note is that the stress correlation has an oscillatory behaviour with a period of about 50 fs. Thus to capture the dynamics of the system well, sampling of MSD should be done at sufficiently small time intervals [38]. For our simulation purpose sampling was done every 5 fs.

2-3 Force fields for Krytox^{TM} oil and its selection for computing transport properties

At the heart of MD simulation are the force field parameters which determine the interaction between different atoms influencing their motion which in turn determines the properties. The interaction among atoms is divided into two classes: bonded and non-bonded. Bonded interactions represent intramolecular bond interaction, which mainly includes bond stretching, bending and torsion depicted in figure 2-3. The non-bonded interactions consist of Lennard-

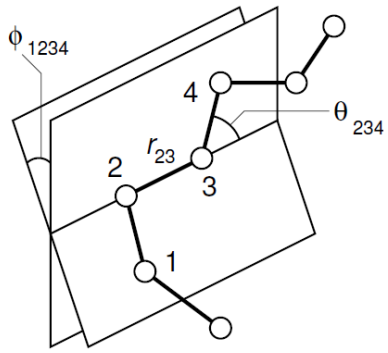

Figure 2-3: Schematic for description of bonded potentials. r_{23} is the bond length representing stretching, θ_{234} is the angle representing bending and ϕ_{1234} is the dihedral angle representing torsion.

Jones (LJ) potential and coulombic potential terms. LJ potential takes into account the van der Waals forces. When the atoms are close to each other they experience attraction because of the positive charge of the nucleus of one atom and the negative charge of the electron cloud of another atom. However, when the electron clouds of two atoms do overlap there is a strong repulsive force known as Pauli repulsion. For computing of forces due to LJ potential, a cut-off distance, generally less than half the simulation box size is implemented. The attractive forces beyond the cut-off distances are corrected by tail correction [14] if the force field specifies else the potential is smoothly transitioned to zero at the cut-off distance. The coulombic potential takes into account the electrostatic charges of the atoms. The range of the electrostatic potential extends well beyond the cut-off distance and in this case, the correction was made by particle-particle particle-mesh (pppm) solver [39] in Fourier space.

For the system of study, the interaction parameters described above were determined from force field data available in the literature. There are various force field models each suitable for specific compounds and property evaluation. The bonded parameters are generally obtained using quantum mechanical calculations, X-ray structure analysis or nuclear magnetic resonance (NMR) spectroscopy. The LJ parameters are obtained using MC simulations to fit experimental densities and heat of vaporization [40]. The way the parameters are determined may vary a bit based on the force field.

The force field parameters have a substantial impact on the property tabulation of a molecule of interest. Various force fields were tested for parameterizing Krytox^{TM} oil molecule. This

section includes the details of force fields and results of the preliminary simulations based on which a particular force field was selected for studying the properties of interest. The details of the simulation are not produced for these preliminary simulations in this section. The procedure was similar as followed for the simulations for the computation of transport properties, the details of which can be found in chapter 3.

2-3-1 Universal force field (UFF)

Universal force field was developed by Rappe et al. [41] with the motive of establishing force field parameters for the entire range of periodic table elements. The parameters of the force field are based only on the element, its hybridization and connectivity. A notable difference in comparison to other force fields is that UFF uses Fourier potential for angles owing to a better description of large amplitude motions whereas harmonic potential is commonly used by other force fields. For simulation of Krytox^{TM} oil, the UFF parameters as adapted by Jiang et al. [24] were utilized. A point of merit is that electric charges are not explicitly accounted for in this force field leading to faster simulation and early convergence for transport properties computation.

The parameter values are listed here as implemented in LAMMPS. The UFF parameters take into account both bonded and non-bonded parameters as shown by equation 2-9, where $\mathcal{U}_{\text{tot}}$ is the total potential energy. Bonded terms include bond stretching ($\mathcal{U}_{\text{R}}$), bond angles bending ($\mathcal{U}_{\theta}$) and dihedral angle torsion potentials ($\mathcal{U}_{\phi}$). The non-bonded term includes Van der Waals forces defined by LJ potential. Partial charges were not explicitly accounted for as their effect was incorporated in other parameters.

$$\mathcal{U}_{\text{tot}} = \mathcal{U}_{\text{R}} + \mathcal{U}_{\theta} + \mathcal{U}_{\phi} + \mathcal{U}_{\text{vdW}} \tag{2-9}$$

Bond stretching potential assumes a harmonic style of the form specified by equation 2-10 with force constant K, equilibrium bond length r_0 and bond distance r.

$$\mathcal{U}_{\text{R}} = K\left(r - r_0\right)^2 \tag{2-10}$$

Bond angle bending potential is expressed by fourier style given by equation 2-11 with θ as the bond angle. The constants C_0, C_1, C_2 are defined by the equilibrium angle (θ_0) using equations 2-12, 2-13, 2-14. A point to note here is that the force field parameters for angle C-C-C were not available in the literature by Jiang et al. The literature for UFF by Rappe et al. [41] was referred for obtaining the parameters. The derivation for it is shown in appendix A.

$$\mathcal{U}_{\theta} = K\left(C_0 + C_1\cos\theta + C_2\cos 2\theta\right) \tag{2-11}$$

$$C_2 = \frac{1}{8\sin^2\theta_0} \tag{2-12}$$

$$C_0 = 4C_2\left(4\cos^2\theta_0 + 3\right) \tag{2-13}$$

$$C_1 = -8C_2\cos\theta_0 \tag{2-14}$$

The energy of torsion represented by dihedral angle (ϕ) is expressed by harmonic potential as shown in equation 2-15. The value of d is 1 for equilibrium dihedral angle $\phi_0 = 180°$.

$$\mathcal{U}_\phi = K\,(1 + d\cos n\phi) \tag{2-15}$$

Finally, the non-bonded interaction which includes only the van der Waals forces takes the form of LJ potential given by equation 2-16 where ε is the magnitude of the potential well representing attraction, σ is the van der Waals diameter and r is the interatomic distance. For atoms of the same molecule, LJ potential was considered only if the atoms were separated by two atoms (equivalent to separation by three bonds). Standard arithmetic mixing rules, $\varepsilon_{ij} = (\varepsilon_i\,\varepsilon_j)^{1/2}$, $\sigma_{ij} = (\sigma_i + \sigma_j)/2$, were used for deriving LJ parameters for atoms of different types. A cut-off distance of 12.5 Å was used for all LJ van der Waals interaction with a correction for long-tail interaction [14]. All the force field parameters as implemented in LAMMPS are listed in table 2-1.

$$\mathcal{U}_{\mathrm{vdW}} = 4\varepsilon\left[\left(\frac{\sigma}{r}\right)^{12} - \left(\frac{\sigma}{r}\right)^{6}\right] \tag{2-16}$$

Jiang et al. [24] studied rheological properties of linear perfluoropolyether $C_8F_{18}O_4$ (CF_3-O-CF_2-CF_2-O-CF_2-CF_2-O-CF_2-CF_2-O-CF_3). Experimental density values and simulated viscosity values for varying shear rates using NEMD simulations are reported in the literature. From the viscosity as a function of shear rate data reported by the authors, zero shear viscosity (Newtonian viscosity) was predicted using polynomial curve fitting [42]. The simulated values from the literature were reproduced using the same force field parameters by EMD simulations in LAMMPS. Both the reproduced simulation and literature results for experimental density and simulated viscosity calculation at the temperature of 333 K and pressure of 1 atm are shown in table 2-2.

For the reproduced simulation, density was under-predicted by 5% and viscosity was under-predicted by a factor of 3. For preliminary results with a single independent MD simulation run these values were considered reasonable enough.

2-3-2 Optimized potential for liquid simulations all-atom (OPLS-AA)

Optimized potential for liquid simulations all-atom force field developed by Jongersen et al. [26] was originally targeted for proteins and has been extended for organic liquids. The charges for OPLS-AA are empirical and are obtained from fitting to reproduce properties of organic liquids. The OPLS-AA force field parameters were reparameterized by Black et al. [25] to reproduce density and heat of vaporization of liquid perfluoropolyether compounds perfluorodiglyme (CF_3-O-(CF_2-CF_2-O)$_2$-CF_3) and perfluorotriglyme (CF_3-O-(CF_2-CF_2-O)$_3$-CF_3). In this text OPLS-AA is referred to the modified force field by Black et al. for which the force field parameter values are listed in appendix B.

Density values for perfluorodiglyme were reproduced by MD simulations in LAMMPS. The simulated values along with those listed in literature are shown in table 2-3. As can be seen, the simulated values are in agreement with the values reported in the literature.

Since the ultimate requirement for the force field was to predict the transport properties, OPLS-AA was utilized for the prediction of viscosity of $C_8F_{18}O_4$ (UFF was used for the same

Table 2-1: UFF force field parameters for Krytox™ oil.

(a) Bond parameters.

Bond type	K (kcal mol^{-1} Å^{-2})	r_0 (Å)
C-C	349.878	1.514
C-O	507.003	1.423
C-F	367.081	1.442

(b) Angle parameters.

Angle type	K (kcal mol^{-1})	θ_0 (°)	C_0	C_1	C_2
C-C-O	300.286	109.47	0.48436	0.37497	0.14062
C-C-F	222.408	109.47	0.48436	0.37497	0.14062
C-O-C	294.384	104.51	0.43361	0.26733	0.13337
F-C-O	275.958	109.47	0.48436	0.37497	0.14062
F-C-F	203.982	109.47	0.48436	0.37497	0.14062
C-C-C	236.528	109.47	0.48436	0.37497	0.14062

(c) Dihedral parameters.

Dihedral type	K (kcal mol^{-1})	ϕ_0 (°)	d	n
X-C-O-X	0.096952	180	1	3
X-C-C-X	1.059495	180	1	3

X: Any atom type.

(d) Lennard-Jones parameters.

Atom type	ε (kcal mol^{-1})	σ (Å)
C	0.105	3.35
F	0.050	2.86
O	0.060	3.00

Table 2-2: Reproduction of properties reported by Jiang et al. [24] for $C_8F_{18}O_4$ at 333 K and 1 atm by simulation using UFF and OPLS-AA force fields.

	Density (kg m^{-3})	Viscosity (cP)
Jiang et al. [24]	1560	1.552
Simulation UFF	1470	0.512
Simulation OPLS-AA	1460	0.538

For the reported literature data, density value is based on experiments whereas viscosity value (at zero-shear) is based on NEMD simulations.

Table 2-3: Reproduction of density values reported by Black et al. [25] for perfluorodiglyme at 1 atm pressure by simulation using OPLS-AA force field.

Temperature (K)	**Density ($kg\,m^{-3}$)**	
	Black et al. [25]	**Simulation OPLS-AA**
293.15	1623	1630
303.15	1593	1585

The values reported in the literature are based on simulations.

molecule in section 2-3-1). The values are listed in table 2-2. The simulated values of density and viscosity by UFF and OPLS-AA are in agreement.

2-3-3 General Amber force field (GAFF)

General Amber force field was developed by Wang et al. [43] and is known for its wide applicability to various organic molecules including those composed of oxygen and halogen atoms. None of the earlier studies has reported the use of GAFF for perfluoropolyether compounds. But owing to its wide applicability it was considered as an option for parameterizing Krytox^{TM} oil.

The partial charges were derived from *ab initio* method using 6-31G* level of theory and fitted using restrained electrostatic potential (RESP) [44] to ensure transferability of charges. R.E.D [45][46] server was used for the two-step procedure of charge derivation. R.E.D uses quantum mechanics (QM) program Gaussian [47] for optimizing the structure of a molecule and generating molecular electrostatic potential (MEP) on a three-dimensional grid. Secondly, the MEP data is transferred to the RESP tool internally for the charge fitting procedure. RESP fitting was performed for both $C_8F_{18}O_4$ (refer section 2-3-1) and perfluorodiglyme (refer section 2-3-2) molecules. For both the molecules density was overpredicted by over 20% as compared to the parent force fields. It was also observed that densities were unaffected by the scaling of charges. The GAFF force field parameters along with the partial charges used for $C_8F_{18}O_4$ molecule are listed in appendix B.

2-3-4 Consistent valence force field (CVFF)

Consistent valence force field was developed by Dauber-Osguthorpe et al. [48] for studying the structure and ligand binding to proteins for a drug-receptor system. The force field parameters were derived based on minimum energy structure study and vibrational spectra analysis for the protein system. Koike [23] utilized CVFF for studying viscosity as a function of shear rate (NEMD) for various perfluorinated polyethers. As a part of the research by Koike, Krytox^{TM} polymeric oil with the number of monomers $n = 4, 9$ was studied.

As per table 1-1, $n = 9$ corresponds to Krytox GPL 102 for which experimental density and viscosity data are available in literature [49][13]. The force field was used for reproducing the experimental density and viscosity of Krytox GPL 102. The force field parameters as adapted by Koike and used for simulations are listed in appendix B. The density values from

the experimental data and as predicted by simulation in LAMMPS are listed in table 2-4. The simulated density value aligns perfectly with the experimental values.

With seemingly good results for density, viscosity was computed by EMD simulations in

Table 2-4: Comparison between the experimental density and those obtained by simulation using CVFF, OPLS-AA and UFF force fields for Krytox GPL 102 at 1 atm pressure.

Temperature (K)	**Density (kg m^{-3})**			
	Experiment [49]	**CVFF**	**OPLS-AA**	**UFF**
297.15	1856	1843	1740	1770

LAMMPS using OCTP tool. It was observed that the viscosity value (figure 2-4) did not converge even after a simulation run of 80 ns. The reason for it is investigated in section 2-3-5.

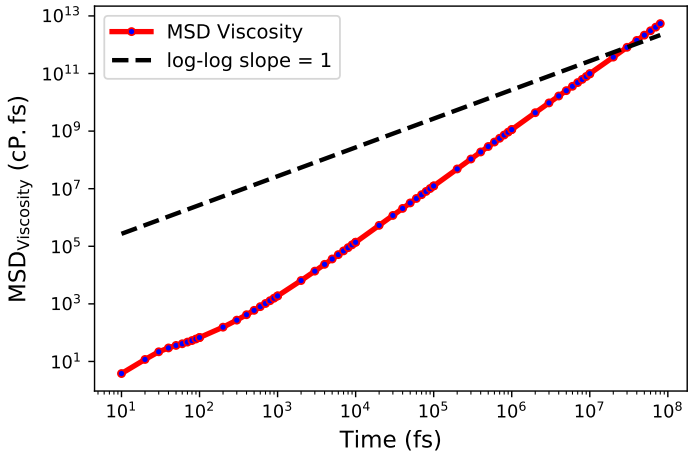

Figure 2-4: MSD plot for computing viscosity of Krytox GPL 102 at 297.15 K temperature and 1 atm pressure using CVFF for a simulation run of 80 ns.

2-3-5 Selection of force field

Four force fields namely UFF, OPLS-AA, GAFF and CVFF were investigated to some extent in the sections above for their suitability for parameterizing Krytox^{TM} oil molecule. It was observed that density of $C_8F_{18}O_4$ and perfluorodiglyme were overpredicted by GAFF and thus it was not investigated further for applicability to Krytox^{TM} oil.

Using the remaining three force fields, the density of Krytox GPL 102 was computed. From table 2-4 it is observed that density is predicted accurately by CVFF whereas by UFF and OPLS-AA it is under-predicted by about 5%.

The value of viscosity did not converge for Krytox GPL 102 (figure 2-4) by using CVFF.

A similar MSD plot was observed for viscosity tabulation using the OPLS-AA force field (not shown here). Whereas for UFF, which does not consist of electric charges, the MSD for viscosity (figure 2-5) converged in 50 ns to a value of 32 cP which is close to the experimental value of 50 cP [49]. It was concluded that long-range electrostatic interactions were responsible for the slow convergence of MSD for viscosity calculation. A point to note here is that MSD plots for viscosity converged for both UFF and OPLS-AA force fields for $C_8F_{18}O_4$ molecule which is a linear chain molecule with low viscosity (refer table 2-2).

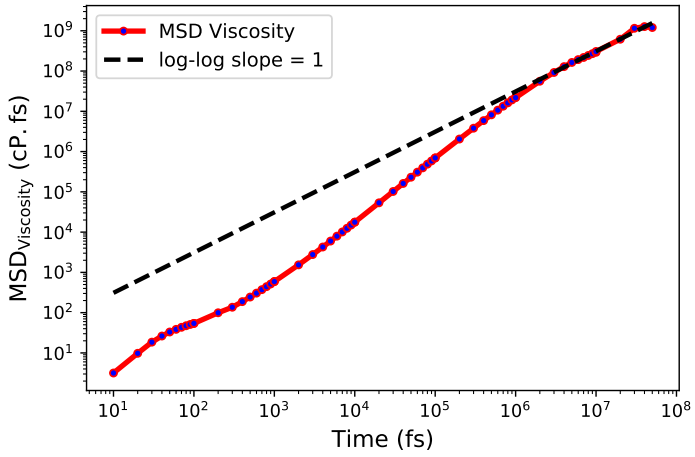

Figure 2-5: MSD plot for computing viscosity of Krytox GPL 102 at 297.15 K temperature and 1 atm pressure using UFF for a simulation run of 50 ns.

Since the convergence rate for viscosity calculation using CVFF and OPLS-AA force fields was slow it was concluded that both models are not of practical use for EMD simulations of highly viscous (and branched) perfluoropolyether compounds like Krytox^{TM} oil. UFF was selected for transport properties prediction of Krytox^{TM} oil using the EMD simulation method.

2-4 Force field parameters for carbon dioxide

For the study of diffusion of CO_2 in oil, a fully flexible EPM2-flex (elementary physical model 2) force field model as described by Zhong et al. [50] was implemented. The authors claim that EPM2-flex is more robust as compared to other fully flexible models MSM-flex and TraPPE-flex (transferable potentials for phase equilibria) and also other rigid models. With EPM2-flex, simulated structural properties and transport properties which include self-diffusivity and viscosity of CO_2 in the liquid state closely represent the experimental values. The bonded and non-bonded parameter styles are the same as that used for Krytox^{TM} oil except the bond angle bending is represented by harmonic potential (equation 2-17). In addition, coulombic potential as described by equation 2-18 (q is the atomic charge and r is the interatomic distance between atoms i and j) is defined for CO_2. The cut-off distance for non-bonded interaction for CO_2 was defined as 14 Å which would only play a role if the number of CO_2 molecules in the system is more than 1. The cut-off distance for LJ potential

for interaction with atoms of oil was defined as 12.5 Å. The long-range electrostatic potential beyond the cut-off distance was resolved using particle-particle particle-mesh (pppm) solver [39] with 10^{-6} units as the accuracy of relative error in forces. The force field parameters as implemented in LAMMPS are listed in table 2-5.

$$\mathcal{U}_{\theta} = K\left(\theta - \theta_0\right)^2 \tag{2-17}$$

$$\mathcal{U}_{\mathrm{el}} = \frac{1}{4\pi\varepsilon_0}\frac{q_i q_j}{r} \tag{2-18}$$

Table 2-5: EPM2-flex force field parameters for CO_2 molecule.

(a) Bond parameters.

Bond type	$\boldsymbol{K}$ **(kcal mol^{-1} Å^{-2})**	$\boldsymbol{r_0}$ **(Å)**
C-O	1283.382	1.149

(b) Angle parameters.

Angle type	$\boldsymbol{K}$ **(kcal mol^{-1})**	$\boldsymbol{\theta_0}$ **(°)**
O-C-O	147.705	180.00

(c) Non-bonded parameters.

Atom type	$\boldsymbol{\varepsilon}$ **(kcal mol^{-1})**	$\boldsymbol{\sigma}$ **(Å)**	$\boldsymbol{q}$ **(e)**
C	0.056	2.76	0.6512
O	0.160	3.03	−0.3256

Chapter 3

Details of atomistic simulations

In section 2-3-5, based on the results of preliminary simulations, it was concluded that the UFF would be the force field of choice for studying properties of Krytox^{TM} oil using EMD simulations. To proceed with the simulations it was required to prepare various simulation files and specify the simulation scheme which includes the main algorithm and boundary conditions. Also, for extensive study of transport properties, systems with oil molecules consisting of a different number of monomers (n) were studied for various temperature and pressure conditions. This chapter describes the details of simulations in sections 3-1, 3-2 and the system configurations of study in section 3-3.

3-1 Simulation preparation

The structure of a single molecule of interest was built using open-access software Avogadro [12][51]. The single-molecule file (.pdb) was used for the preparation of the initial system configuration with randomly arranged molecules in a cubic box using Packmol software [52]. The output data file (.pdb) from Packmol was made compatible with LAMMPS by executing the script *make_lammps.tcl* in VMD (Visual MD) [53]. *data.system* was the topology file obtained from VMD and it served as one of the input files to LAMMPS. Atom coordinates, simulation box size and other geometric details about bonds, angles and dihedrals were part of this file. Another input file to LAMMPS called *forcefield.data* file consisted of all the force field parameter details specified in section 2-3-1. The input files *data.system* and *forcefield.data* were invoked by the main *Simulation.in* file, the contents of which are described in section 3-2.

3-2 Simulation scheme

As described earlier, LAMMPS [27], an open-source molecular dynamic simulator program was used for simulation purpose. *Simulation.in*, the main input file to the software included

all the details described here. Periodic boundary conditions were applied in all three directions to simulate properties of the fluid in bulk by avoiding wall effects. To determine the attributes associated with the atoms, *atom_style* was chosen as *full* which includes all the molecular and charge details. For efficient computing, *Newton's third law* was switched *on* for pairwise and bonded interaction. To integrate Newton's equation of motion, the Velocity Verlet algorithm [14] was used with a time step of 1 fs.

The following steps were followed to compute the properties:

- To prevent overlapping of atoms, energy minimization was performed using conjugate gradient method [14] for 1000 steps setting maximum movement of a single atom to 0.05 Å in a single iteration. The stopping tolerances for energy and force were set to 10^{-4} and 10^{-6} units respectively.
- MD equilibration run in isothermal-isobaric (NPT) ensemble was performed for 1 ns. The system temperature was maintained using Nose-Hoover thermostat [54] acting every 100 timesteps and pressure was maintained using Nose-Hoover barostat acting every 1000 timesteps. A lower frequency for barostatting (as compared to thermostatting) is set to avoid high fluctuations in pressure and thus the volume of the simulation box.
- MD production run in isothermal-isobaric (NPT) ensemble was performed for 5 ns to compute the average box volume that would be used for a run in NVT ensemble (this could be considered as an extended equilibration run as no transport properties were computed here).
- MD equilibration run in canonical (NVT) ensemble was performed for 0.1 ns. At the beginning of the run, the simulation box dimensions were scaled to average box volume calculated from the production run in the NPT ensemble. The system temperature was maintained using Nose-Hoover thermostat [54] every 100 timesteps.
- All the transport properties were computed in production run in microcanonical (NVE) ensemble using OCTP tool, the details for which are described in section 2-2. The length of the run was 50 ns (for some systems a longer run was carried out and is indicated separately). At the beginning of the run, atom velocities were scaled to the temperature of interest. For diffusivity and viscosity, MSDs were sampled every 1000 and 5 timesteps respectively. In addition, RDFs were calculated using OCTP tool, corrected for finite-size effects [55][56]. The bin size of 1000 was used for RDFs (the distance between the centre of an atom and the cut-off distance was divided into 1000 parts).

For calculation of diffusion coefficient, the sampling frequency of MSD every 1000 timesteps was sufficient as atom positions were calculated at every timestep regardless. For viscosity calculation, frequent sampling every 5 timesteps was required because of high fluctuation in the terms of the pressure tensor (and hence capture the effects of short correlation time) [38]. The simulation methodology is summarized by the flowchart in figure 3-1.

The sufficiency of 1 ns NPT equilibration run was tested based on equilibration of system energy, density, the average molecular radius of gyration and average molecular end to end distance. Statistics for a system with 25 oil molecules with a number of monomers $n = 9$ in a molecule are presented here. From figure 3-2a and 3-2b it can be seen that the system is

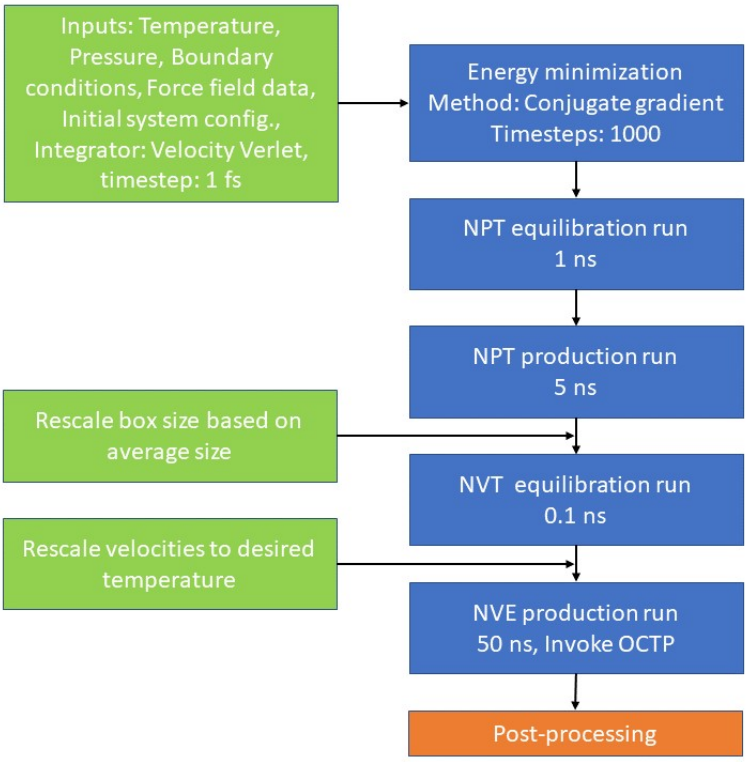

Figure 3-1: Flow diagram for MD simulation methodology as implemented in LAMMPS.

equilibrated in terms of energy and density. Also based on figure 3-2c the structure of the molecule is sufficiently relaxed. Further relaxation of the structure takes place in the NPT production run.

3-3 Simulation conditions for different types of Krytox^{TM} oil

In the previous sections, the simulation preparation method and run procedure were described. The viscosity of Krytox^{TM} oil molecule and diffusivity of CO_2 in the oil for various temperatures, pressures and polymer chain lengths have been studied. This section provides details of the conditions of the study.

For this project, several independent systems each with molecules of a particular type of Krytox^{TM} oil (based on the number of monomers in a chain) and containing a specified number of oil molecules in a simulation box were studied as listed in table 3-1. The number of molecules for a particular system was decided based on avoiding any nonphysical interactions. Nonphysical interactions imply the motion of one end of a polymer getting affected by the other end of the same molecule through a periodic boundary. For a system type K9 with number of monomers $n = 9$ and number of molecules = 25, radius of gyration and end to end distance were found to be 7.84 Å and 21.03 Å respectively (at operating temperature of 323.15 K and pressure of 1 atm). The length of the cubic box was about 34.4 Å. The difference between end to end distance of a oil molecule and the box length is more than the

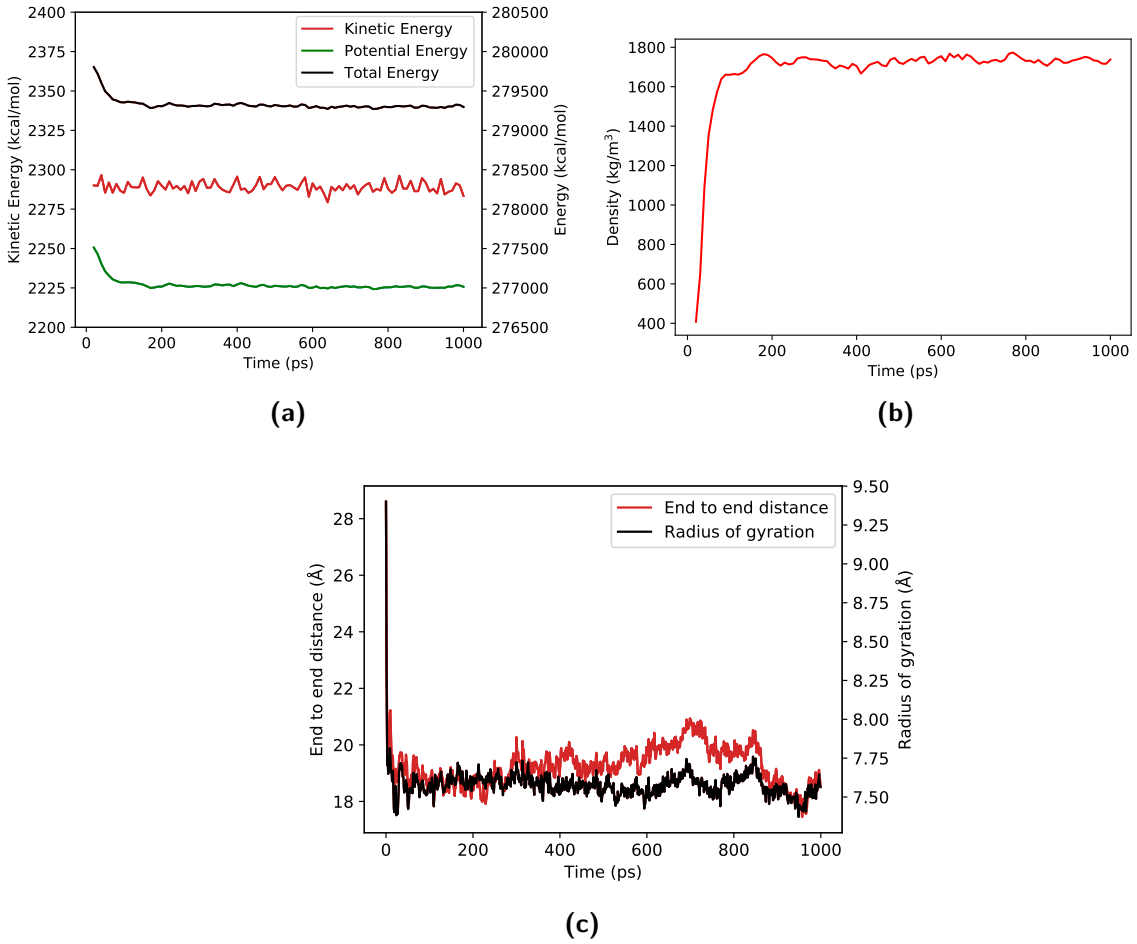

Figure 3-2: Equilibration run of 1 ns in an NPT ensemble for a system with 25 oil molecules with number of monomers $n = 9$ at 323.15 K temperature and 1 atm pressure using UFF: (a) Energy profile; (b) Density profile; (c) Relaxation of molecule geometry.

cut-off distance of 12.5 Å. This alone is not a sufficient criterion to conclude the occurrence of nonphysical effects as there could be long-range interactions. RDF between C atom of oil and C, F, O atoms of the oil is plotted at 323.15 K and 1 atm in figure 3-3. It can be seen that beyond a distance of about 7 Å the value of correlation function $g(r)$ is 1 which means that the atoms are uncorrelated. In addition, for the same system, simulations were performed with the number of oil molecules = 50 and similar density and viscosity values were obtained (not shown here).

For all the systems, simulations were carried out at pressure of 1 atm and temperature values 293.15 K, 313.15 K and 343.15 K. For systems with oil type K8 and above, simulations for viscosity did not converge in 50 ns run for the temperature of 293.15 K and thus results for them are not shown. In addition, for systems with type K6 oil which corresponds to Krytox GPL 101 (refer tables 1-1 and 3-1) simulations were carried out at a pressure of 2398 atm and temperature of 533 K as experimental values are available in the literature [13]. For type K9 oil which corresponds to Krytox GPL 102 simulations were carried out (including the additional operating condition specified for type K6 oil) for temperature values of 297.15 K,

Table 3-1: System definition based on the molecule type with different number of monomers and number of molecules of the particular type in a simulation box.

Abb.	No. of monomer units in a molecule	No. of Krytox^{TM} oil molecules
K4	4	45
K6	6	35
K8	8	30
K9	9	25
K10	10	32
K13	13	55

K6 corresponds to Krytox GPL 101.
K9 corresponds to Krytox GPL 102.
K13 corresponds to Krytox GPL 103.

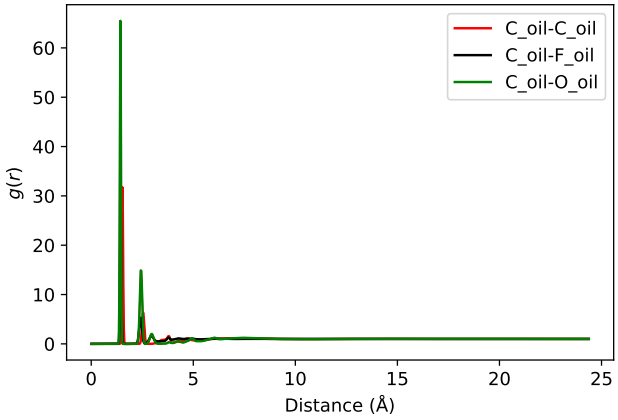

Figure 3-3: RDFs calculated between C atom and C, F, O atoms of type K9 oil at 323.15 K temperature and 1 atm pressure using UFF.

323.15 K and pressure values at 1 atm, 83 atm, 122.4 atm and 193.4 atm for the availability of experimental data in literature [49].

For all the systems 1 CO_2 molecule per simulation box for temperature upto 313.15 K and 2 CO_2 molecules per simulation box for temperatures above 313.15 K were considered [1]. The reason for 2 CO_2 molecules at higher temperature was to improve statistics. It was observed that at higher temperatures CO_2 varied for different independent simulation runs. This is attributed to ergodicity. Thus to improve the statistics, 2 CO_2 molecules were considered.

Experimental values of CO_2 diffusivity in Krytox GPL 101 at pressure values of 1 atm, 10 atm and temperature values of 293.15 K, 323.15 K are available from the work of Dr H. Bazyar, performed at P&E laboratory, TU Delft. Thus for those systems, simulations were performed to predict diffusivity of CO_2.

[1] for systems at pressure of 2398 atm and temperature of 533 K, 1 CO_2 molecule per simulation box was considered.

Since a particular grade of oil is always a mixture of different polymeric molecules of various chain lengths, simulations were also carried out for different mixtures corresponding to Krytox GPL 101 and Krytox GPL 102 as shown in table 3-2. The selection of types of polymeric chain length (based on the number of monomers) to include for a particular grade of oil for a mixture was arbitrary. Simulations were performed for pressure of 1 atm and temperature values of 293.15 K and 313.15 K.

Table 3-2: System definition of Krytox™ oil mixture considered for simulation based on Krytox GPL type it represents.

Krytox® GPL	**Abb.**	**Details**	**Mixture ratio**	n_{avg}	**Exp.** n_{avg} **[13]**
101	K468	Mixture of K4, K6, K8	12:12:6	6.26	6.28
102	K613	Mixture of K6, K13	35:35	9.50	9.53

A ratio of 12:12:6 for K468 corresponds to 12 molecules of type K4, K6 oil each and 6 molecules of type K8 oil in a simulation box.

Chapter 4

Results of atomistic simulations using UFF for Krytox^{TM} oil

This chapter fulfils the major objective of the project by studying the diffusivity of CO_2 in Krytox^{TM} oil and viscosity of oil for conditions of varying polymer chain length, temperature and pressure and comparing it to the available experimental data. The chapter is divided into four sections. Sections 4-1 and 4-2 are explicitly dedicated to reporting simulated properties of Krytox GPL 101 Krytox GPL 102 respectively and comparing them to the available experimental data. Section 4-3 reports the simulated properties (and experimental if available) for various chain lengths of Krytox^{TM} oil molecule and analyzes the effect of chain length on properties. Structural properties of the oil are investigated in section 4-4.

For each condition of temperature, pressure and number of oil molecules of a particular type in a box, five independent simulation runs based on different initial configurations were performed. For viscosity of oil and diffusivity of CO_2 in oil calculation, the MSDs for diffusivity and oil viscosity obtained from five independent runs were combined and averaged respectively to generate an additional data point. The reported mean density is based on five data points and reported mean oil viscosity and CO_2 diffusivity in oil is based on six data points. The reported CO_2 diffusivity in the oil has been corrected for finite-size effects using equation 2-6 by considering the mean simulated oil viscosity for correction purpose (correction in CO_2 diffusivity was observed to be within 2.5%). The reported uncertainty is calculated at 95% confidence interval. A point to note here is that the reported simulated densities are with 1 or 2 (refer section 3-3) dissolved CO_2 molecules. The difference in density of pure oil and with dissolved CO_2 was observed to be less than 2%.

4-1 Simulation results and experimental validation of properties for Krytox GPL 101 oil

For simulations, pure oil of type K6 (refer table 3-1) and oil mixture of type K468 (refer table 3-2) corresponds to Krytox GPL 101. Type K6 oil was studied for a range of temperature

and pressure values whereas type K468 was studied only to a limited extent mainly to understand whether the predicted properties of type K468 oil are in agreement with the simulated properties of type K6 oil.

All the simulation and experimental data for density, viscosity and diffusivity of CO_2 in the oil are consolidated in table 4-1. The experimental values of diffusivity of CO_2 in oil were obtained from the work of Dr H. Bazyar, performed at P&E laboratory, TU Delft. Fick's diffusivity was calculated by Dr H. Bazyar by equation 4-1 [7] based on the solubility data of CO_2 in Krytox GPL 101. This experimental value of diffusivity was utilised for comparing the diffusivity obtained from MD simulations.

$$< C >= C_{\mathrm{S}} \left[1 - 2 \left(1 - \frac{C_0}{C_{\mathrm{S}}} \right) \sum_{n=0}^{\infty} \frac{\exp\left(-\lambda_n^2 D t\right)}{L^2 \lambda_n^2} \right] \tag{4-1}$$

where:

$< C >$ = Space-averaged concentration at time t
C_{S} = Saturation concentration
C_0 = Initial concentration
λ_n = Eigenvalue
D = Solute diffusivity
L = Depth of oil in the container

For a better understanding of the data several plots are generated for which the observations are listed below:

- In figure 4-1a density as a function of temperature is plotted. The simulated densities are under-predicted mainly owing to the lower well depth (attractive forces are proportional to the well depth) of LJ potential. Nonetheless, the simulated values of densities follow the same trend as experimental values.
- From figure 4-1b it can be seen that density (ρ) values satisfy equation 4-2 for thermal expansion coefficient (α_p).

$$\alpha_p = \frac{1}{\rho} \left(\frac{\partial \rho}{\partial T} \right)_p \tag{4-2}$$

- As seen in figure 4-2a, viscosity, though under-predicted, consistently decreases with temperature. Greater variation between the simulated and experimental values is observed at a lower temperature. A point of observation is that with an increase in temperature the uncertainty in viscosity reduces because of a faster convergence of Einstein's relation (equation 2-7), resulting in more data for converged state for the same length of the simulation.
- In plot 4-2b it is seen that viscosity (η) follows Arrhenius relation (η_0 is the pre-exponential factor) as suggested by literature [57] of the form given by equation 4-3.

$$\eta(T) = \eta_0 \exp\left(\frac{\text{slope}}{T} \right) \tag{4-3}$$

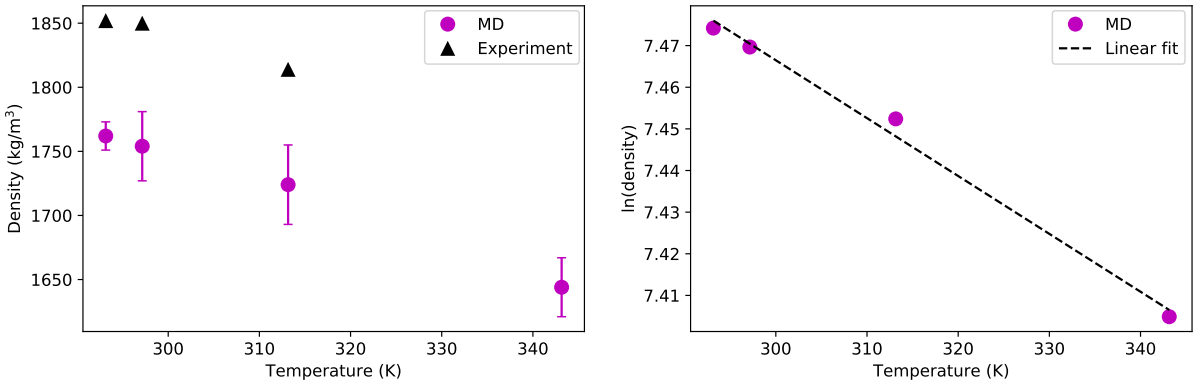

Figure 4-1: (a) Comparison between the experimental density of Krytox GPL 101 and simulated density of type K6 oil for varying temperature at 1 atm pressure; (b) Thermal expansion coefficient is determined from the slope.

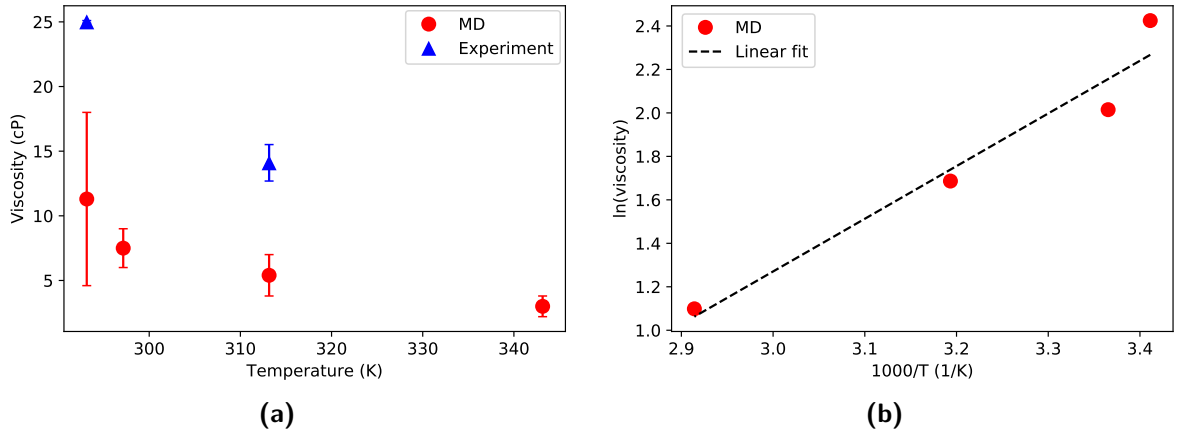

Figure 4-2: (a) Comparison between the experimental viscosity of Krytox GPL 101 and simulated viscosity of type K6 oil for varying temperature at 1 atm pressure; (b) Arrhenius plot for simulated oil viscosity.

- The diffusivity of CO_2 increases linearly with temperature as shown in figure 4-3. This can be accredited to the Stokes-Einstein equation (equation 4-4), where diffusivity (D) is proportional to temperature. Diffusivity is a function of viscosity (η) which is also a function of temperature (exponential form) but these are weakly coupled. An additional point to note is that at high temperature the uncertainty in CO_2 diffusivity is more because of exploration of the phase space (there might be various local minima for the energy state where the system is trapped). Thus for higher temperature, 2 CO_2 molecules are considered per simulation box for improving the statistics.

$$D = \frac{k_B T}{6\pi\eta r} \tag{4-4}$$

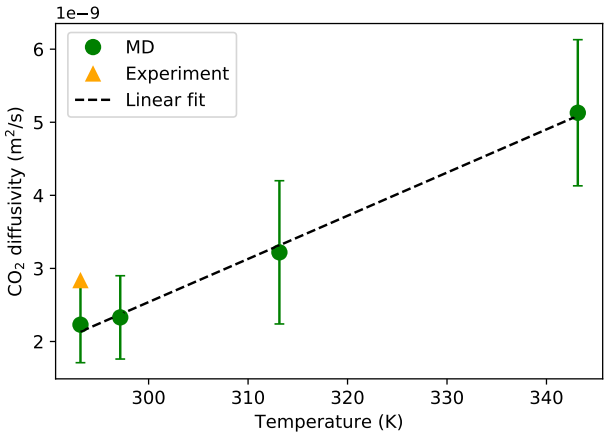

Figure 4-3: Comparison between the experimental and simulated CO_2 diffusivity in Krytox GPL 101 and type K6 oil respectively for varying temperature at 1 atm pressure.

For diffusivity of CO_2 in type K6 oil it was observed that the simulated values are in agreement with the experimental values at lower pressure (serial no. 1, table 4-1). Although at high pressures the deviation is significant (serial no. 5 and 6). Also, experimental data predicts an increase in CO_2 diffusivity with an increase in pressure whereas with pressure the diffusivity is expected to reduce as predicted by MD simulations.

For the oil mixture, it is seen that simulation results for type K468 closely resembles simulation results for type K6 (serial no. 1 and 3) for all the reported properties.

Table 4-1: Simulated and experimental properties of Krytox GPL 101.

No.	Temp. (K)	Pressure (atm)	Density ($kg\,m^{-3}$)			Viscosity (cP)			CO_2 diffusivity ($m^2\,s^{-1}$)		
			K6	K468	Exp.	K6	K468	Exp.	K6	K468	Exp.
1	293.15	1	1762 ± 11	1743 ± 26	1852 [11]	11.3 ± 6.7	9.3 ± 4.1	25.0 ± 0.1 [58]	$2.23 \pm 0.52 \times 10^{-9}$	$2.45 \pm 0.33 \times 10^{-9}$	2.84×10^{-9}
2	297.15	1	1754 ± 27		1850 [58]	7.5 ± 1.5			$2.33 \pm 0.57 \times 10^{-9}$		
3	313.15	1	1724 ± 31	1702 ± 25	1814 [11]	5.4 ± 1.6	5.7 ± 0.8	14.1 ± 1.4 [11]	$3.22 \pm 0.98 \times 10^{-9}$	$3.17 \pm 0.81 \times 10^{-9}$	
4	343.15	1	1644 ± 23			3.0 ± 0.8			$5.13 \pm 1.00 \times 10^{-9}$		
5	293.15	10	1765 ± 28			11.3 ± 6.6			$2.13 \pm 0.36 \times 10^{-9}$		1.39×10^{-8}
6	323.15	10	1699 ± 24			4.1 ± 2.5			$4.16 \pm 1.76 \times 10^{-9}$		1.77×10^{-8}
7	533.00	2398	1856 ± 10			11.1 ± 3.2		16.9 ± 0.8 [13]	$2.81 \pm 0.50 \times 10^{-9}$		

Mean values are reported with uncertainty calculated at 95% confidence interval.
Uncertainty data for experimental density and CO_2 diffusivity are not available for all the operating conditions and is thus not reported.

4-2 Simulation results and experimental validation of properties for Krytox GPL 102 oil

Krytox GPL 102 is used as a reference fluid for viscosity measurements of hydrocarbons and thus a wide range of experimental data is available for it [49][13]. Because of the availability of experimental data, extensive simulations are carried out for the study of this particular grade of Krytox^{TM} oil. For simulations, pure oil of type K9 (refer table 3-1) and oil mixture of type K613 (refer table 3-2) corresponds to Krytox GPL 102. Type K9 oil was studied for a wide range of temperature and pressure values whereas type K613 was studied only to the limited extent mainly to understand whether the predicted properties of type K613 oil are in agreement with the properties of type K9 oil.

All the simulation and experimental data for density, viscosity and diffusivity of CO_2 in the oil are consolidated in table 4-2. For a better understanding of the data, several plots were generated. Observations made for variation of properties concerning change in temperature values are listed below:

- In figure 4-4a density as a function of temperature is plotted. The simulated densities are under-predicted as compared to the experimental values for the same reason as specified for type K6 oil (refer section 4-1). Nonetheless, the simulated values of densities follow the same trend as experimental values. At the temperature of 343.15 K, it seems that the difference in experimental and simulated value is increasing but the small drift is because of the 2 CO_2 molecules in the simulation box at a higher temperature. Also, it is interesting to note that high uncertainty in simulated density is observed at a temperature of 323.15 K. This is merely a matter of poor statistics because ideally the fluctuations should have varied only based on the number of oil molecules in a simulation box which is the same for all the simulations. This fluctuation appeared with doping of 2 CO_2 molecules in the simulation box (instead of 1). From figure 4-4b it can be seen that density values satisfy equation 4-2 for thermal expansion coefficient.
- As seen in figure 4-5a, viscosity, though under-predicted, consistently decreases with temperature. Greater variation between the simulated and the experimental value is observed at lower temperatures. This is anticipated because viscosity decays exponentially as a function of temperature [57] (here also referred to as Arrhenius relation) whereas the governing LJ potential follows a power law.
- In plot 4-5b it is seen that viscosity follows Arrhenius relation as suggested by literature [57] of the form given by equation 4-3. This relation could be used to predict viscosity at higher temperatures.
- The diffusivity of CO_2 increases linearly with temperature as shown in figure 4-6 and is in agreement with the Stokes-Einstein equation (equation 4-4).

There are also some trends seen in oil properties and CO_2 diffusivity for variation in pressure. The observations are listed below:

- As expected density of the oil increases with pressure as seen in figure 4-7a. The simulated values are lower as compared to the experimental values for the same reason as mentioned for temperature variation plots.

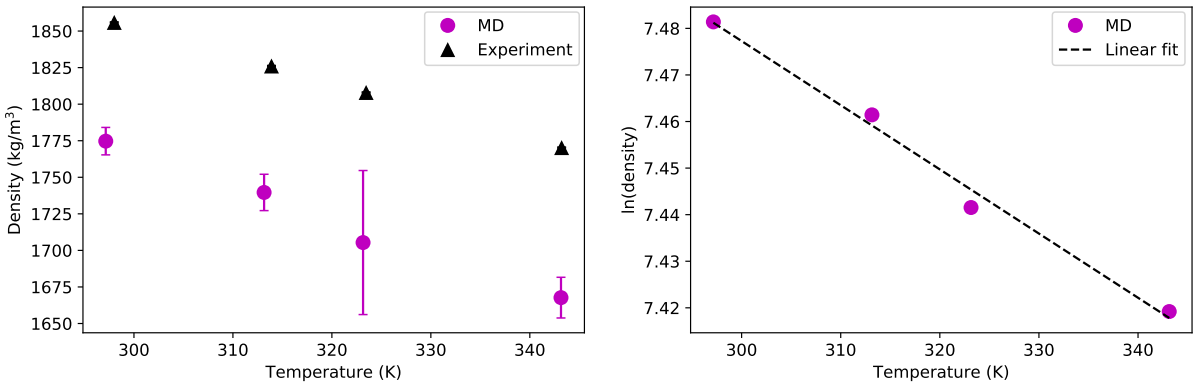

Figure 4-4: (a) Comparison between the experimental density of Krytox GPL 102 and simulated density of type K9 oil for varying temperature at 1 atm pressure; (b) Thermal expansion coefficient is determined from the slope.

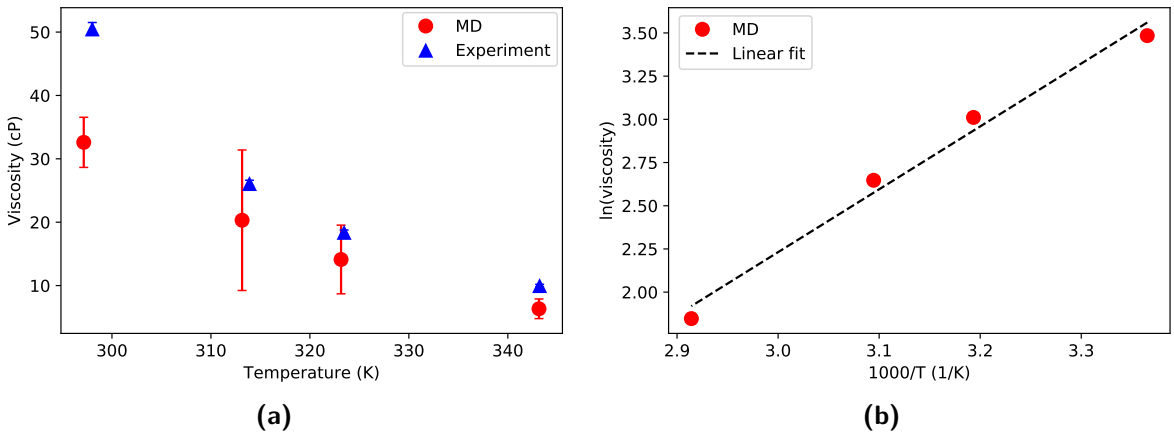

Figure 4-5: (a) Comparison between the experimental viscosity of Krytox GPL 102 and simulated viscosity of type K9 oil for varying temperature at 1 atm pressure; (b) Arrhenius plot for simulated oil viscosity.

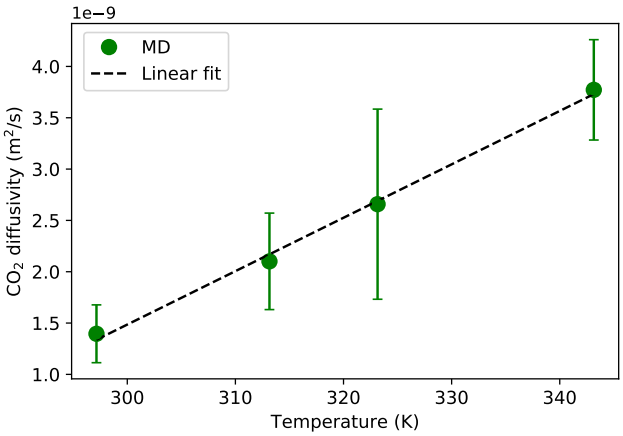

Figure 4-6: Simulation results for CO_2 diffusivity in type K9 oil for varying temperature at 1 atm pressure.

- From figure 4-7b it can be seen that density values satisfy equation 4-5 for isothermal compressibility (κ_T).

$$\kappa_T \equiv -\frac{1}{\rho}\left(\frac{\partial \rho}{\partial p}\right)_T \tag{4-5}$$

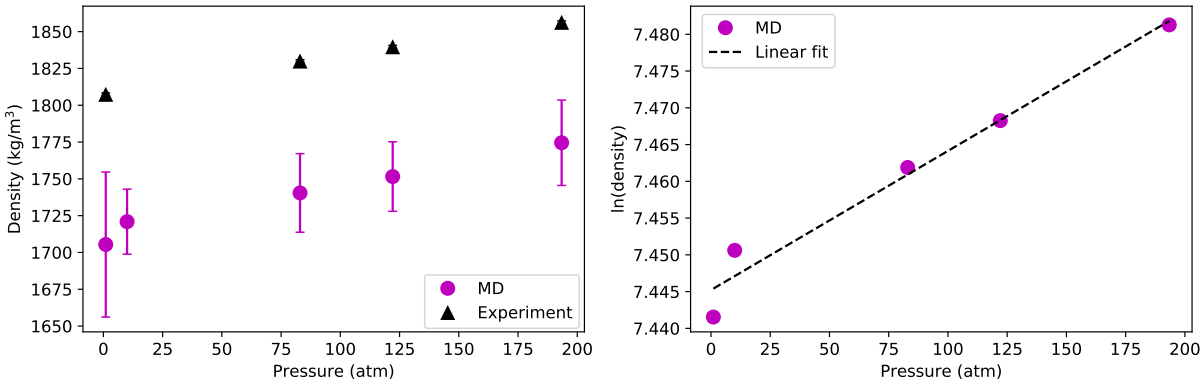

Figure 4-7: (a) Comparison between the experimental density of Krytox GPL 102 and simulated density of type K9 oil for varying pressure at 323.15 K temperature; (b) Isothermal compressibility is determined from the slope.

- Viscosity increases with an increase in pressure (figure 4-8) because of the increased shearing between the molecules. Higher uncertainty in viscosity is observed at higher pressures because of the higher fluctuations in pressure tensor components. Also, at higher pressure as the viscosity increases the convergence of Einstein's relation (equation 2-7) is slow. Thus at higher pressures, there is less data for the converged state for the same length of the simulation. Like exponential relation for variation viscosity with

temperature, there are no generalized correlations for relating pressure to the viscosity of a liquid [59].

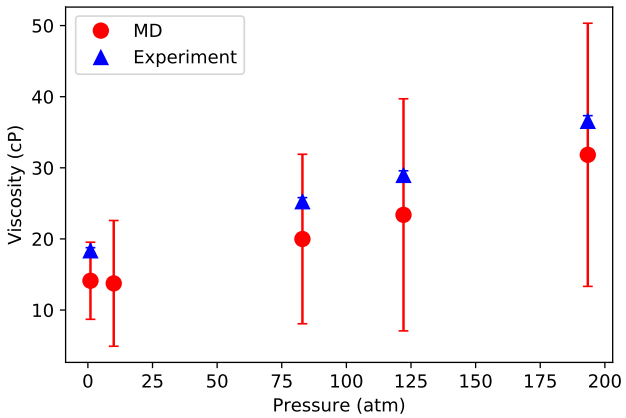

Figure 4-8: Comparison between the experimental viscosity of Krytox GPL 102 and simulated viscosity of type K9 oil for varying pressure at 323.15 K temperature.

- As seen in figure 4-9, the diffusivity of CO_2 in oil decreases as the pressure increases but stagnates at higher pressures because of the close packing of oil molecules.

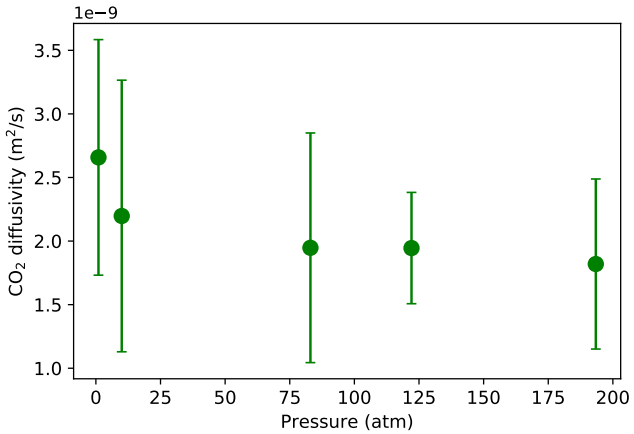

Figure 4-9: Simulation results of CO_2 diffusivity in type K9 oil for varying pressure at 323.15 K temperature.

The above observations are noted for simulations of type K9 oil and its comparison with experimental data for Krytox GPL 102. For the oil mixture, it is seen that results for type K613 resemble more closely the experimental data (serial no. 3, table 4-2) both in terms of density and viscosity. Prediction of CO_2 diffusivity in type K613 oil is of the same order of magnitude as for type K9 oil.

Table 4-2: Simulated and experimental properties of Krytox GPL 102.

No.	Temp. (K)	Pressure (atm)	Density ($kg\,m^{-3}$)			Viscosity (cP)			CO_2 diffusivity ($m^2\,s^{-1}$)	
			K9	K613	Exp. [49]	K9	K613	Exp. [49]	K9	K613
1	293.15			1795 ± 8	1865 ± 1		47.6 ± 42.7	62.8 ± 1.3		$1.17 \pm 0.40 \times 10^{-9}$
2	297.15	1	1775 ± 9		1856 ± 1	32.6 ± 3.9		50.5 ± 1.0	$1.39 \pm 0.28 \times 10^{-9}$	
3	313.15	1	1740 ± 12	1755 ± 21	1826 ± 1	20.3 ± 11.1	25.1 ± 11.7	26.1 ± 0.5	$2.10 \pm 0.47 \times 10^{-9}$	$1.91 \pm 1.13 \times 10^{-9}$
4	323.15	1	1705 ± 49		1808 ± 1	14.1 ± 5.4		18.4 ± 0.4	$2.66 \pm 0.93 \times 10^{-9}$	
5	343.15	1	1668 ± 14		1770 ± 1	6.3 ± 1.5		10.0 ± 0.2	$3.77 \pm 0.49 \times 10^{-9}$	
6	323.15	10	1721 ± 22			13.7 ± 8.8			$2.20 \pm 1.07 \times 10^{-9}$	
7	323.15	83	1740 ± 27		1830 ± 1	19.9 ± 11.9		25.2 ± 0.5	$1.95 \pm 0.90 \times 10^{-9}$	
8	323.15	122	1752 ± 24		1840 ± 1	23.4 ± 16.3		29 ± 0.6	$1.94 \pm 0.44 \times 10^{-9}$	
9	323.15	193	1775 ± 29		1856 ± 1	31.8 ± 18.5		36.6 ± 0.7	$1.82 \pm 0.67 \times 10^{-9}$	
10	533.00	2398	1864 ± 14		1979 [13]	32.9 ± 22.3		27.3 ± 1.3 [13]	$1.87 \pm 0.68 \times 10^{-9}$	

The temperature values for the experimental data is not exact and might vary by a maximum of 0.8 K.
The reported experimental data is from the source referenced in the header section unless explicitly stated.
Mean values are reported with uncertainty calculated at 95% confidence interval.

4-3 Simulation results for Krytox^{TM} oil for varying chain length

Simulations for varying chain length of Krytox^{TM} oil molecule at different temperatures were performed to study the behaviour of change in oil viscosity and CO_2 diffusivity in the oil. This could be of interest for selecting a particular grade of oil for SLMs. All the simulation and experimental data for density, viscosity and diffusivity of CO_2 in the oil are consolidated in tables 4-3 and 4-4. The property trends for variation in chain length and/or temperature are captured in the various plot, a brief description for which is summarized below:

- As expected density increases with chain length (figure 4-10) because of an increase in the ratio of the total number of bonds to the total number of atoms inside the simulation box. It is observed that density variation is minimal for type K8, K9 and K10 oil. Also, the rate of increase in density decreases for the higher chain lengths as compared to the lower ones.

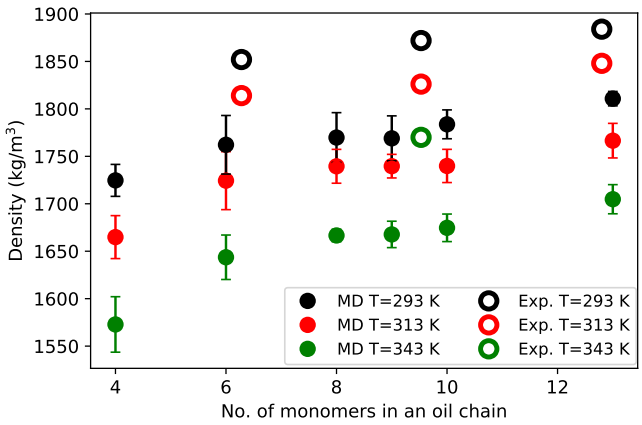

Figure 4-10: Comparison between the experimental and simulated density of Krytox^{TM} oil for different temperatures and varying chain length at 1 atm pressure.

- A quadratic increase in oil viscosity is observed with an increase in chain length as can be seen in figure 4-11. This is attributed to the intertwining of polymer chains as the length increases. The higher uncertainty in viscosity at higher chain lengths is attributed to slow convergence leading to poor statistics for the same duration of the simulation run.
- For systems with oil type K8 and above, at the temperature of 293 K, MSD for viscosity calculation did not converge for a simulation production run of 50 ns attributed to the inertia of the system. Thus, the viscosity values are not reported (figure 4-11a).
- For diffusivity of CO_2 in oil, the same trend (inverse) as for density variation is observed as can be seen in figure 4-12. Higher uncertainty in CO_2 diffusivity for a smaller chain length is attributed to the exploration of phase space (ergodicity).

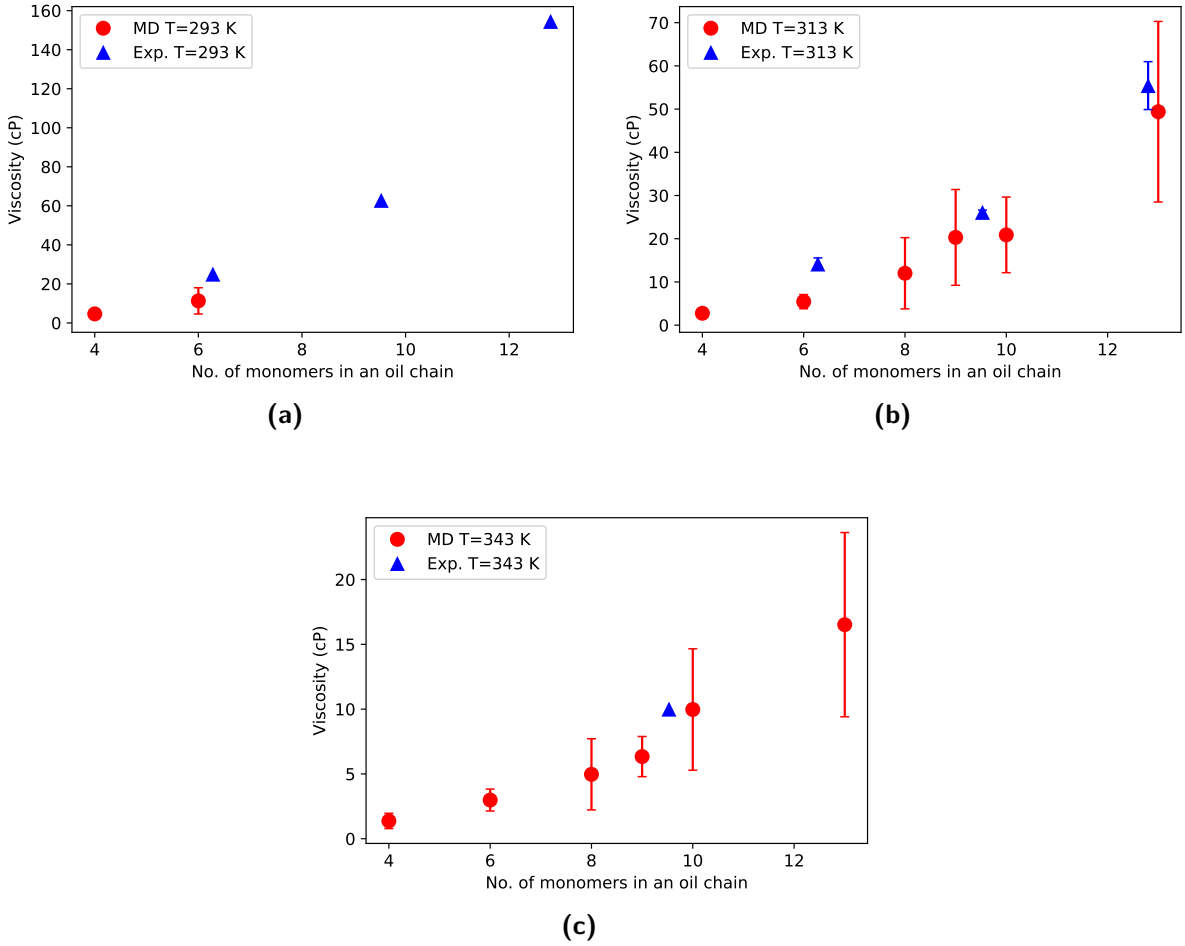

Figure 4-11: Comparison between the experimental and simulated viscosity of Krytox^{TM} oil for varying chain length at 1 atm pressure: (a) 293 K; (b) 313 K; (c) 343 K.

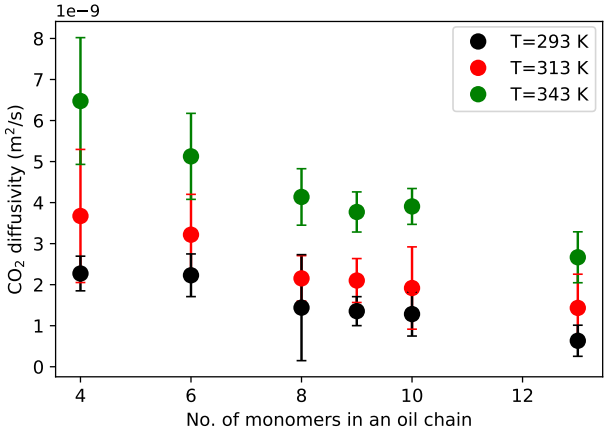

Figure 4-12: Simulation results of CO_2 diffusivity in Krytox^{TM} oil for different temperatures and varying chain length at 1 atm pressure.

Table 4-3: Simulated properties of Krytox™ oil for varying chain length at 1 atm pressure.

Temperature (K)	Property	K4	K6	K8	K9	K10	K13
293.15	Density	1725 ± 17	1762 ± 31	1770 ± 26	1769 ± 24	1784 ± 15	1811 ± 8
	Viscosity	4.6 ± 1.8	11.3 ± 6.7				
	CO_2 diffusivity	$2.27 \pm 0.42 \times 10^{-9}$	$2.23 \pm 0.52 \times 10^{-9}$	$1.44 \pm 1.29 \times 10^{-9}$	$1.35 \pm 0.35 \times 10^{-9}$	$1.28 \pm 0.54 \times 10^{-9}$	$6.33 \pm 3.79 \times 10^{-10}$
313.15	Density	1665 ± 23	1724 ± 31	1739 ± 18	1740 ± 12	1740 ± 18	1767 ± 18
	Viscosity	2.8 ± 1.0	5.4 ± 1.6	12.0 ± 8.2	20.3 ± 11.1	20.9 ± 8.7	49.4 ± 20.9
	CO_2 diffusivity	$3.67 \pm 1.62 \times 10^{-9}$	$3.22 \pm 0.98 \times 10^{-9}$	$2.15 \pm 0.55 \times 10^{-9}$	$2.10 \pm 0.53 \times 10^{-9}$	$1.92 \pm 1.0 \times 10^{-9}$	$1.43 \pm 0.82 \times 10^{-9}$
343.15	Density	1573 ± 29	1644 ± 23	1667 ± 6	1668 ± 14	1675 ± 14	1705 ± 15
	Viscosity	1.4 ± 0.6	3.0 ± 0.8	5.0 ± 2.7	6.3 ± 1.6	10.0 ± 4.7	16.5 ± 7.1
	CO_2 diffusivity	$6.48 \pm 1.54 \times 10^{-9}$	$5.13 \pm 1.1 \times 10^{-9}$	$4.14 \pm 0.69 \times 10^{-9}$	$3.77 \pm 0.49 \times 10^{-9}$	$3.91 \pm 0.43 \times 10^{-9}$	$2.67 \pm 0.62 \times 10^{-9}$

Units: Density ($kg\,m^{-3}$), Viscosity (cP), CO_2 diffusivity ($m^2\,s^{-1}$)
For type K13 oil at 313.15 K, NVE simulation run was performed for 70 ns.
Mean values are reported with uncertainty calculated at 95% confidence interval.

Table 4-4: Experimental properties of Krytox™ oil for varying chain length at 1 atm pressure.

Temperature (K)	Property	GPL 101	GPL 102	GPL 103
293.15	Density	1852 [11]	1872 [49]	1884 [11]
	Viscosity	25.0 ± 0.1 [58]	62.8 ± 1.3 [49]	154.5 ± 15.4 [11]
313.15	Density	1814 [11]	1826 [49]	1848 [11]
	Viscosity	14.1 ± 1.4 [11]	26.1 ± 0.5 [49]	55.4 ± 5.5 [11]
343.15	Density		1770 [49]	
	Viscosity		10.0 ± 0.2 [49]	

Mean values are reported with uncertainty calculated at 95% confidence interval.
Uncertainty data for experimental density is not available for all grades of oil and is thus not reported.

4-4 Structural properties of Krytox^{TM} oil

All the macroscopic properties of substances have their origin at a microscopic level and studying those might be useful in deducing the macroscopic behaviour and properties.

The average radius of gyration and end to end distance for a pure oil type (with a fixed number of monomers) and polymer chains in a mixture with uncertainty calculated at 95% confidence interval are tabulated in table 4-5. As per the Flory-Huggins model [60] (valid for ideal polymers), a polymer chain will always prefer a coiled state because it results in minimum free energy (a state of maximum entropy). This is also valid for real polymer chains. All the different types of Krytox^{TM} oil molecules have adhered to this theory (coiled state of type K9 oil molecule is shown in figure 4-13) except for type K4 oil molecule which prefers chain stretching as shown in figure 4-14. The molecular interactions and resulting velocity gradients are responsible for overcoming the energy barrier and leading to chain stretching (another point deduced here is that smaller chains have higher self diffusivity than longer chains).

Another interesting point was observed for polymer chains in oil mixtures. In type K468 oil which is a mixture of polymer chains with the number of monomers $n = 4$, 6, 8, molecules with $n = 8$ showed stretching when compared to type K8 oil (which only has polymer chains with $n = 8$). Similarly for type K613 oil which is a mixture of polymer chains with the number of monomers $n = 6$, 13, molecules with $n = 13$ showed stretching when compared to type K13 oil (which only has polymer chains with $n = 13$). This stretching of longer polymer chains in presence of shorter polymer chains is attributed to the higher self diffusivity of short-chain molecules. The results are depicted in figure 4-15.

Table 4-5: Geometric details obtained from simulations for oil with different chain lengths at 313.15 K temperature and at 1 atm pressure.

Oil type	Subtype	Radius of gyration (Å)	End to end distance (Å)
K4		5.37 ± 0.41	15.22 ± 2.70
K6		5.81 ± 0.54	14.21 ± 4.71
K8		6.97 ± 1.14	18.11 ± 7.74
K9		7.84 ± 1.68	21.03 ± 11.71
K10		8.94 ± 1.41	25.30 ± 8.39
K13		10.04 ± 2.77	27.22 ± 15.92
K468	K4	5.40 ± 0.40	15.39 ± 2.59
	K6	5.82 ± 0.53	14.08 ± 4.53
	K8	11.23 ± 5.70	20.90 ± 11.49
K613	K6	5.83 ± 0.58	14.04 ± 4.88
	K13	10.46 ± 2.67	29.27 ± 14.73

Mean values are reported with uncertainty calculated at 95% confidence interval.

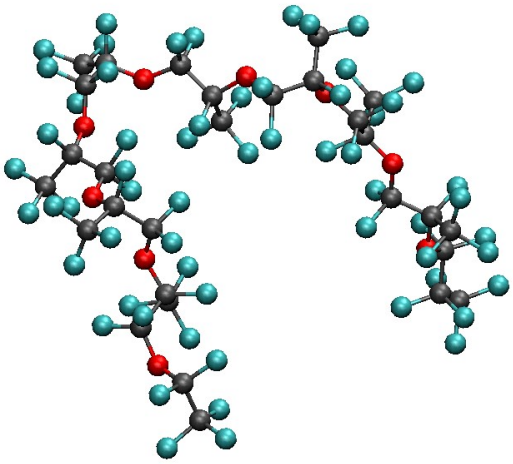

Figure 4-13: Coiled structure of K9 type oil molecule. Oxygen atoms are red, carbon atoms are black, fluorine atoms are blue (figure produced using VMD software [53]).

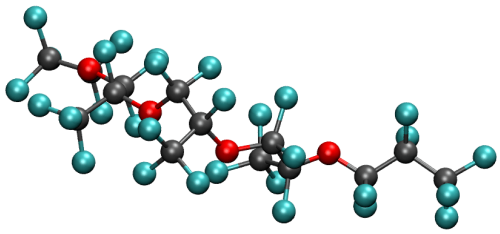

Figure 4-14: Stretched structure of K4 type oil molecule. Oxygen atoms are red, carbon atoms are black, fluorine atoms are blue (figure produced using VMD software [53]).

In addition to studying the structural properties of the oil, the behaviour of CO_2 in oil was studied. RDFs were calculated between the carbon atom of CO_2 and atoms of oil and between the oxygen atom of CO_2 and atoms of oil for type K9 oil as shown in figure 4-16. The repulsion between the oxygen atom of CO_2 and the fluorine atom of oil is evident from RDF shown in figure 4-16b.

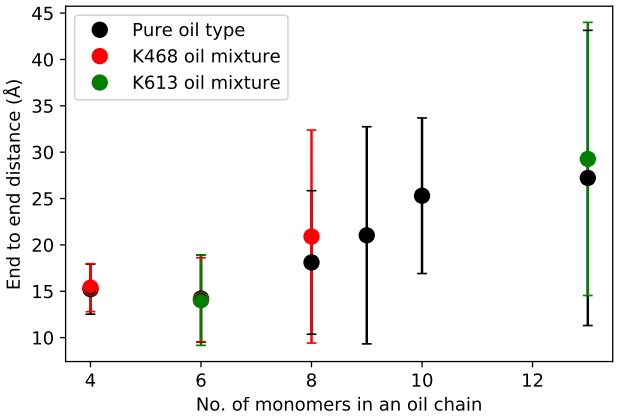

Figure 4-15: End to End distance for varying chain length for simulations at 313.15 K temperature and 1 atm pressure.

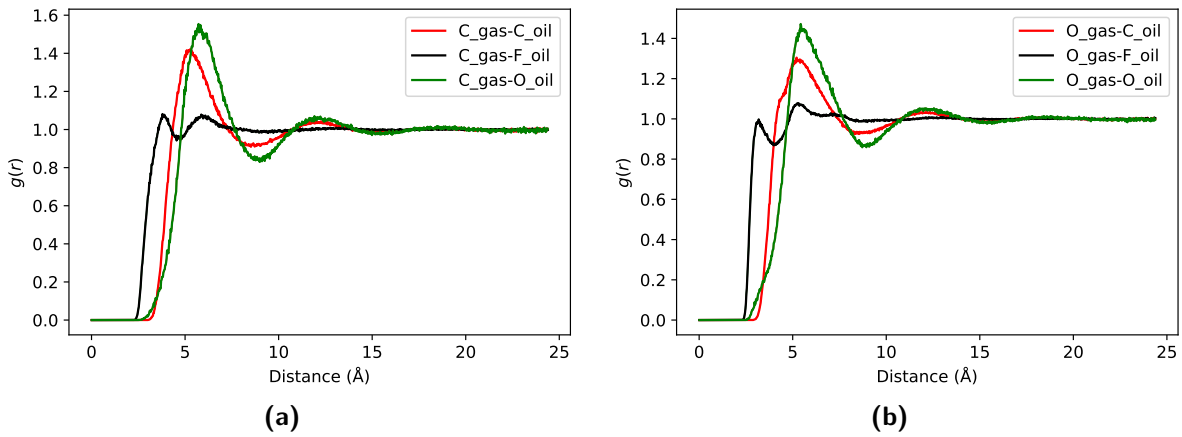

Figure 4-16: RDFs calculated for CO_2 in type K9 oil at 343.15 K temperature and 1 atm pressure: (a) C atom of CO_2 and C, F, O atoms of oil; (b) O atom of CO_2 and C, F, O atoms of oil.

Chapter 5

Coarse-graining of Krytox^{TM} oil molecule

In chapter 4, the results obtained using the AA model (also known as the atomistic model) with the UFF model were discussed. As specified, the property tabulation was carried out in an NVE ensemble with a simulation run of 50 ns. Each simulation run lasted for about 3-5 days when run on a supercomputer (with 12-28 core processors). To increase the computational efficiency, coarse-graining of the molecule was carried out using the MARTINI force field [61]. This reduced the simulation time from days to a few hours or even minutes. A point to note here is that like atomistic MD simulations are not a total substitute for experiments, in the same way, the coarse-grained (CG) models are not a substitute for AA models. Not all details can be studied with CG models but longer time scales of a system can be explored.

CG models involve mapping a small number of atoms and representing it by a single interaction site (here referred to as a bead). The sites interact mainly via short-range LJ potential. Also, a timestep of the order 20-40 fs is possible for CG simulations. These are the main reasons for the computational efficiency of CG models. CG models were originally developed by Marrink et al. [62] for lipid and surfactant systems. The calibration of the building blocks of the model was done by performing an analysis of partition free energies linked to the chemical functional groups. Throughout the years the applicability of the MARTINI force field has widened to many organic compounds. The recent release of the MARTINI 3 [29] force field has incorporated the possibility to parameterize halogenated compounds. This chapter includes details on parameterizing and performing simulations for a perfluoropolyether molecular system using the MARTINI force field. Also, the performance analysis of the results obtained from CG simulations is compared to the results obtained using atomistic simulations.

5-1 Parameterizing a molecule for MARTINI force field

This section describes the general procedure for parameterizing a molecule using the MARTINI force field. The first step to run a CG simulation requires the mapping of atoms into beads. This involves grouping atoms of a molecule that serve as a single interaction site. Based on the type of atoms in a bead, a bead type is assigned to it. The bead type is mainly about allocating LJ potential parameters as specified by the MARTINI force field.

MARTINI force field does not explicitly include the values for the bonded parameters. Thus for obtaining them, performing an atomistic simulation is a pre-requisite. The mapping carried out for a molecule is imposed on the trajectory file obtained from atomistic simulation. This provides bond and angle distribution data which are used for specifying equilibrium bond and angle values for the CG model (parameterizing of dihedral parameters was not carried out for this project) for the MARTINI force field. The force constant values for bonds and angles are provided initially with arbitrary values. After running CG simulations, the bond and angle distributions are tabulated. If they do not match with the data from the mapped trajectory of atomistic simulation, the force constants are optimized. Once the bond and angle parameters are optimized, the density (or other thermodynamic property) of the system is calculated and compared with the experimental value. If this is not in coherence with the experiments, the bead type or the mapping specified is changed and the simulations are performed again until the desired accuracy is reached. The methodology for CG simulations using the MARTINI force field is summarized in flow chart 5-1.

5-2 Mapping of a Krytox^{TM} oil molecule and details of simulation

Simulations using the MARTINI force field were performed for type K6 (Krytox GPL 101) and K9 (Krytox GPL 102) oil (refer table 3-1). Identical mapping was done for both the molecules to ensure the transferability of all force field parameters. First, the atomistic simulations were performed on type K6 oil. Assigning of bead type (determines the LJ parameters) and obtaining bonded parameters was done for type K6 oil. The parameters were then transferred to type K9 oil (the entire procedure was also repeated separately for type K9 oil to ensure that the same bonded force field parameters and distributions were obtained as transferred from type K6 oil). This section describes the details of the mapping procedure, simulation procedure and calculation of transport properties.

5-2-1 Mapping and obtaining of force field parameters for MARTINI force field

Mapping was done as shown in figure 5-2 where each bead is represented by a red box. After many iterations of CG simulations for obtaining the desired density of the oil, the bead type was fixed as type *X3*. Bead type *X3* is for halogenated compounds and is suitable for a molecule that is neither too hydrophilic nor possesses a high ability for self-interaction. Bead masses were specified as the sum of the atomic masses for all the atoms in the particular bead. No charges were assigned to the beads.

As can be seen in figure 5-2, four bond types were defined, two types for terminal bonds (*bond_term1*, *bond_term2*) and two types for core bonds (*bond_core1*, *bond_core2*). Three

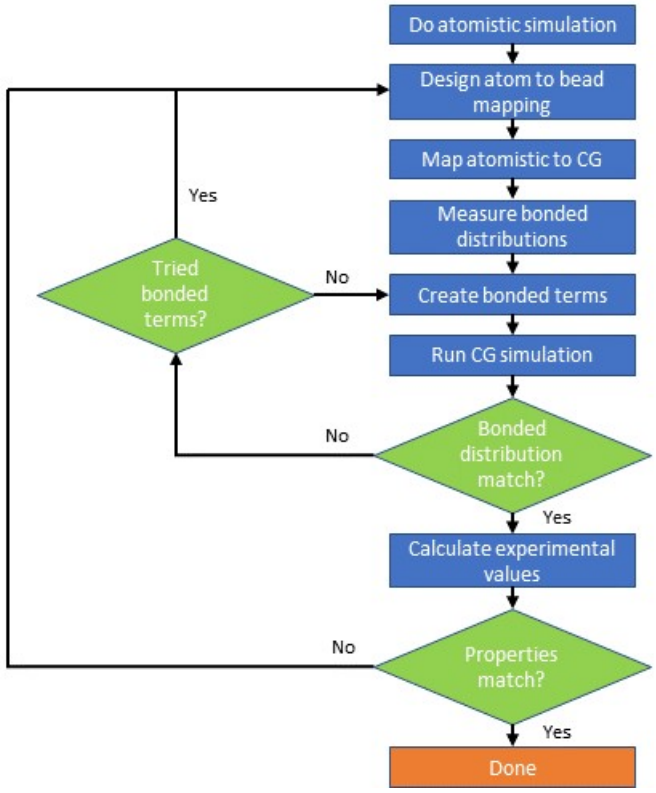

Figure 5-1: CG simulation methodology using the MARTINI force field.

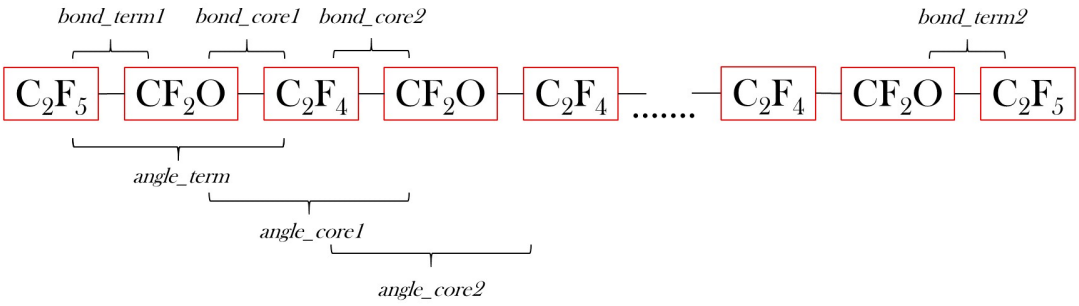

Figure 5-2: Mapping of Krytox^{TM} oil molecule for CG simulations using the MARTINI force field. Red box represents bead type *X3*. Terminal bonds are represented by *bond_term1* and *bond_term2*. Core bonds are represented by *bond_core1* and *bond_core2*. Terminal angles are represented by *angle_term*. Core angles are represented by *angle_core1* and *angle_core2*.

types of angles were defined, one type for terminal angle (*angle_term*) and two types for core angles (*angle_core1*, *angle_core2*). For obtaining all the bonded parameters first atomistic simulations were performed with 50 type K6 oil molecules in a box. Simulations were performed using GROMACS [30]. OPLS-AA force field as developed by Jorgensen et al. [26] was implemented for its availability in GROMACS (please do not confuse the OPLS-AA with the OPLS-AA by Black et al. [25] utilized in section 2-3-2). The force field parameters used are specified in appendix C. Simulation procedure for atomistic simulation was similar to that

described in section 3-2 and thus the details are not provided here (the major difference is that the simulation run was not performed in an NVE ensemble as transport properties were not computed using atomistic simulations).

The trajectory file from the atomistic simulation was mapped to a CG trajectory as per the mapping scheme defined above. Mapping was done using the CGbuilder tool [63] to obtain the index file of the mapped trajectory. Few iterations of CG simulations (the procedure is described in section 5-2-2) were carried out to obtain optimum bonded parameters. Bonds were defined by harmonic potential using equation 5-1 and angles were defined by harmonic potential using equation 5-2. The optimized bonded parameters are listed in table 5-1.

$$\mathcal{U}_{\mathrm{R}} = \frac{1}{2} K \left(r - r_0\right)^2 \tag{5-1}$$

$$\mathcal{U}_{\theta} = \frac{1}{2} K \left(\theta - \theta_0\right)^2 \tag{5-2}$$

Table 5-1: Bonded force field parameters for coarse-grained Krytox™ oil for the MARTINI force field.

(a) Bond parameters.

Bond type	$\boldsymbol{K}$ **(kJ mol^{-1} nm^{-2})**	$\boldsymbol{r_0}$ **(nm)**
bond_core1	6800	0.291
bond_core2	21000	0.275
bond_term1	30500	0.263
bond_term2	8000	0.291

(b) Angle parameters.

Bond type	$\boldsymbol{K}$ **(kJ mol^{-1})**	$\boldsymbol{\theta_0}$ **(°)**
angle_core1	90	75.4
angle_core2	90	147.2
angle_term	90	146.2

The bond and angle distributions obtained using these parameters and their comparison to the mapped trajectory from the atomistic simulation are shown in figures 5-3 and 5-4. Most of the bond and angle distributions from CG simulation matched well with the distributions obtained from the mapped atomistic trajectory. The reasons for exceptions are specified below:

- High value of force constants were provided for *bonds_term1* and *bonds_core2* (refer table 5-1a) in spite of which it was not possible to meet the steep distribution of mapped AA as shown in figures 5-3b and 5-3c. Although the distributions for the CG model seem reasonable enough, bond constraints could be provided if required (not provided in this case).

- In figure 5-4a it is seen that the angle distribution for *angle_core1* has shifted over 20°. This is because of the larger bead size of CG simulation. No possible solution is anticipated for this scenario other than using a smaller bead type (this has shown a substantial increase in density of the system beyond the desired value and is thus not a preferred alternative).

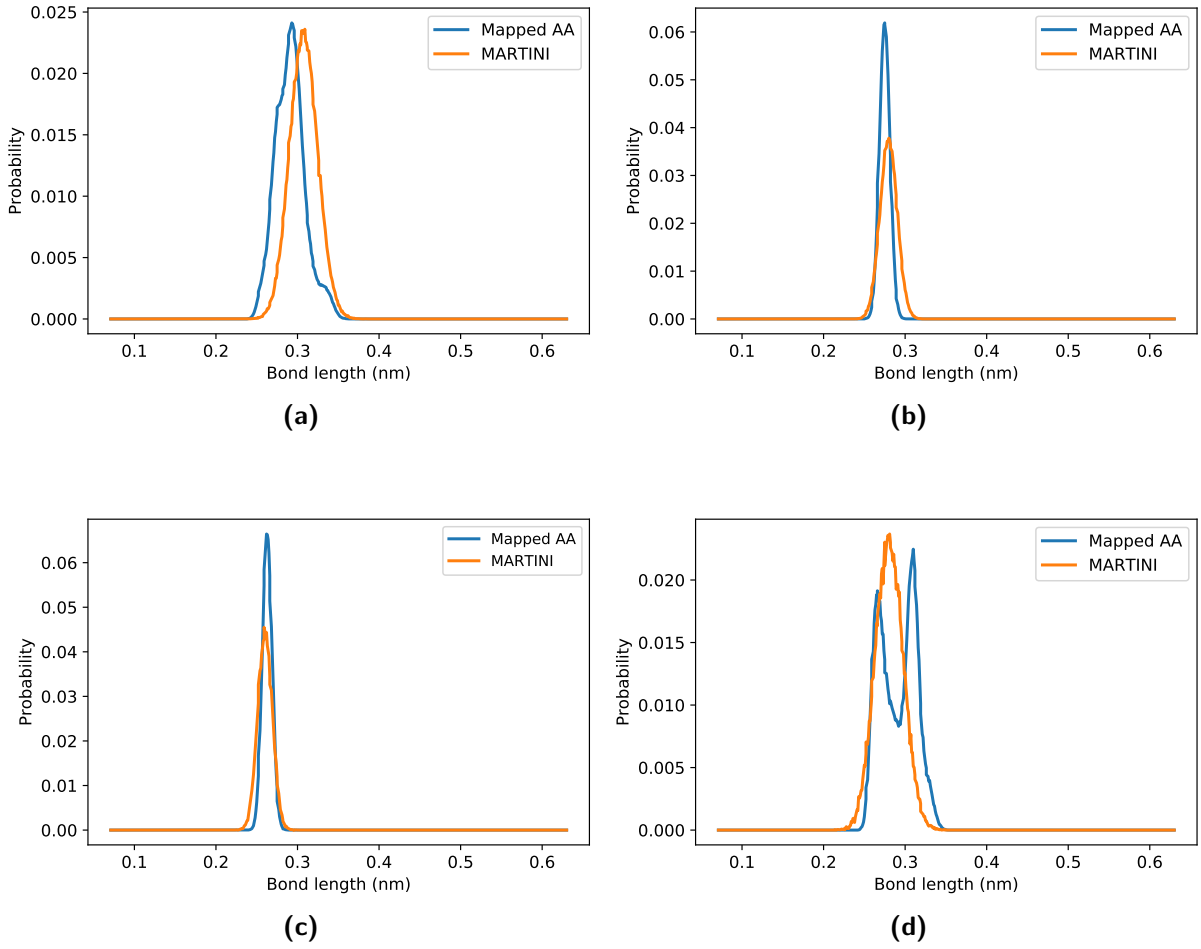

Figure 5-3: Bond distributions for mapped atomistic trajectory and trajectory from CG simulation using the MARTINI force field. Types: (a) *bond_core1*; (b) *bond_core2*; (c) *bond_term1*; (d) *bond_term2*.

For CO_2, bead type *N3r* representing nonpolar bead with reduced self interaction was implemented. Two CO_2 molecules per bead were considered.

5-2-2 Simulation scheme

As described earlier, GROMACS protocol [30], an open-source molecular dynamic simulator program was used for simulation purpose. 50 CG oil molecules with periodic boundary conditions in all three directions occupied the box. The Verlet neighbour search algorithm

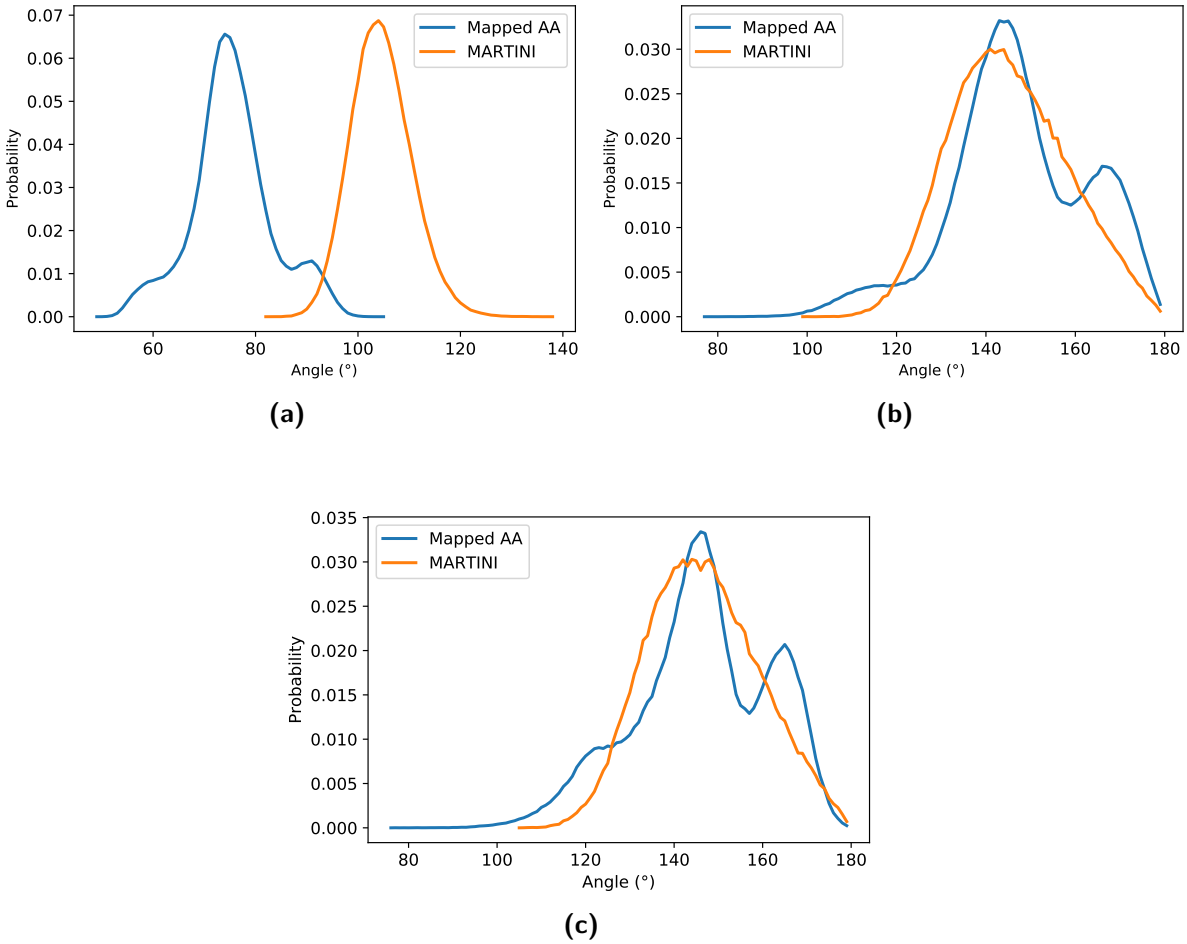

Figure 5-4: Angle distributions for mapped atomistic trajectory and trajectory from CG simulation using the MARTINI force field. Types: (a) *angle_core1*; (b) *angle_core2*; (c) *angle_term*.

[64] was used to update the neighbour list every 20 steps with a buffer tolerance of 0.005 kJ mol^{-1} ps^{-1}. For LJ terms, cut-off scheme with a value of 1.1 nm and Verlet cut-off scheme for potential-shift [65] were used. Using MARTINI, non-bonded interaction is excluded only with the neighbouring beads. A timestep of 20 fs was implemented for all simulations.

Simulations were carried out following the steps in the order listed below:

- The mapped trajectory from the last timestep of the atomistic simulation was used as an input to CG simulation for initial system configuration. Energy minimization was performed using the steepest descent method [14] for 5000 steps.
- MD equilibration run in NPT ensemble was performed for 10 ns. Leap-frog algorithm [14] for integrating Newton's equation of motion was implemented. For temperature control, velocity rescaling thermostat [66] with a coupling time constant of 1 ps was implemented. For pressure control isotropic pressure coupling using Berendsen barostat [14] with a time constant of 3 ns and compressibility of 0.0003 bar^{-1} was used

(Parrinello-Rahman barostat [67] was unstable with high value of force constants for bonded terms).

- MD production run was performed in NVT ensemble for 200 ns. Velocity Verlet algorithm [14] for integrating Newton's equation of motion was implemented. System temperature was maintained using Nose-Hoover [54] thermostat with a time constant of 4 ps.

5-2-3 Transport properties calculation by CG simulations using the MARTINI force field

The transport properties namely oil viscosity and diffusivity of CO_2 in oil were calculated using Einstein relation (refer section 2-2). The viscosity of oil was calculated indirectly. The self-diffusivity of oil was calculated, and then using the Stokes-Einstein equation (given equation 4-4), viscosity was calculated. The hydrodynamic radius (r) was considered as the average radius of gyration of the molecule. This is a valid assumption for systems at low pressure [68].

The direct method for viscosity computation required sampling the energy of the system (which includes the virial terms) every 10 timesteps (200 fs). Also, the longer simulation runs as compared to those performed for calculation of self-diffusivity of oil were required. This consumed substantial disk space (in the order of 2000 Mbs). Also, the post-processing of the file using a Python [69] script for viscosity tabulation was computationally intensive (processing of about 0.5 million data points). Nonetheless for one of the simulations, for type K9 oil, viscosity was calculated in a direct manner using Einstein relation. Viscosity was obtained as 220.8 cP which is close to the value obtained from the indirect computation which is 239.8 cP (details in section 5-3). On the contrary, position vectors for diffusivity calculation were sampled every 10000 timesteps (200 ps). In chapter 4, it was noted that correction of diffusivity for finite-size effects was about 2.5% (maximum). For CG simulation a bigger system was considered as compared to atomistic simulation in chapter 3 (50 type K9 oil molecules instead of 25 molecules for the atomistic model using UFF), thus the finite-size effects for diffusivity computation were further reduced. For validation, CG simulations were also carried out with 200 CG oil molecules in a simulation box and the oil self-diffusivity obtained was the same as that for 50 molecules in a box (<1% difference, the results are not shown here).

5-3 Simulation results and its validation with atomistic simulation and experimental data

CG simulations were performed for type K6 and K9 oil and the results were compared to the experimental data and the results obtained from the study of atomistic simulations using UFF (refer chapter 4). 50 coarse-grained oil molecules (type K6 or K9) were considered along with 2 CO_2 molecules (1 bead) in a simulation box. The system was studied for operating conditions of 1 atm pressure and temperatures of 293.15 K and 313.15 K.

For each system configuration, five independent simulation runs were performed. The reported property values are the mean values with uncertainties reported at 95% confidence interval.

All the simulation and experimental data for density, viscosity and diffusivity of CO_2 in the oil are consolidated in table 5-2. For a better understanding of the data, several plots are generated. Observations made for variation of properties for change in temperature values are listed below:

- In figure 5-5, densities for type K6 and K9 oil are plotted. As can be seen, density values by CG simulation are over-predicted by about 10% as compared to the experimental data. Density calculated for type K6 oil is higher than type K9 oil, although the difference is not much. This ideally should not have been the case. The density values were calculated on the last timestep of NPT run (unlike for atomistic simulations in LAMMPS where density was determined based on the average value of the simulation box size for certain timesteps) and are anticipated as one of the reasons for this variation.

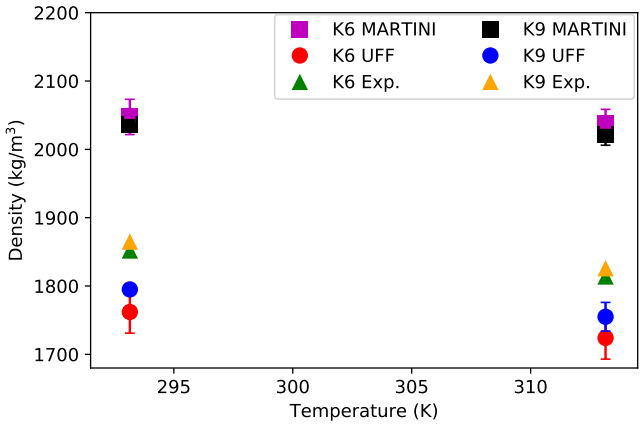

Figure 5-5: Comparison between the experimental and simulated (both CG using MARTINI and AA using UFF) density of Krytox™ oil of type K6 (represents Krytox GPL 101), K9 (represents Krytox GPL 102) oil for varying temperature at 1 atm pressure.

- In figure 5-5 it is also observed that change in density with temperature is more gentle for CG simulations as compared to AA simulation results and experimental data. This is attributed to the depth of the well of LJ potential which is about four times the well depth for the atomistic force field model. This difference in potential well size leads to a higher gradient of potential ($\mathcal{U}$) in equation 5-3 for the CG model which then affects the pressure (P) and thus the density.

$$P = \frac{Nk_{\mathrm{B}}T}{V} - \frac{1}{3V}\sum_{i=1}^{N}\sum_{j>i}^{N}\left\langle r_{ij}\left(\frac{d\mathcal{U}\left(r_{ij}\right)}{dr_{ij}}\right)\right\rangle \tag{5-3}$$

- From logarithmic plots in figures 5-6a and 5-6b it is observed that viscosity is highly overestimated by CG simulations. An observation was made that at the temperature

of 293.15 K, oil viscosity varied with a factor of 20 for type K6 and K9 oil as compared to the experimental values. For the temperature of 313.15 K oil viscosity varied with a factor of 9 for type K6 and K9 oil as compared to the experimental values. Although the statistics are not sufficient, these correlations could be used to predict Krytox^{TM} oil viscosity for different chain lengths at the same operating conditions of temperature and pressure.

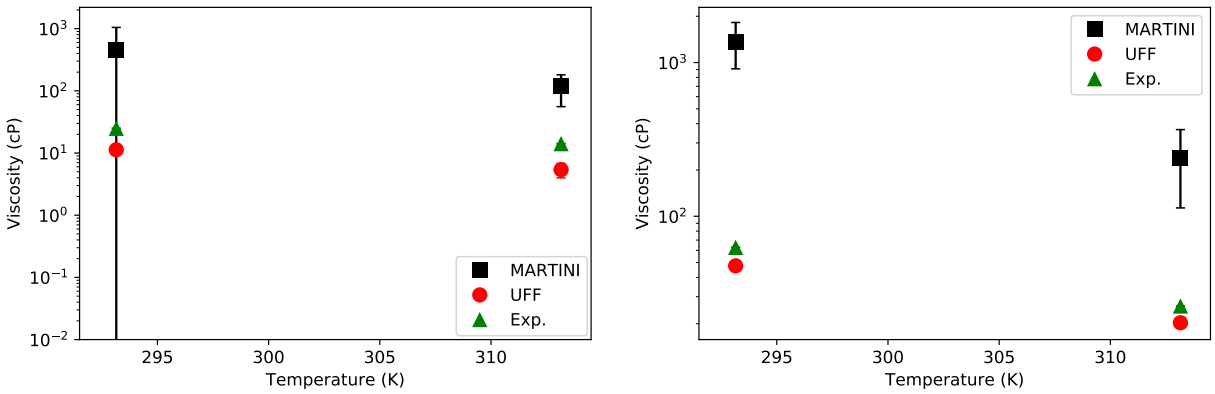

Figure 5-6: Comparison between the experimental and simulated (both CG using MARTINI and AA using UFF) viscosity of Krytox^{TM} oil for varying temperature at 1 atm pressure: (a) Type K6 oil; (b) Type K9 oil.

- From logarithmic plots in figures 5-7a and 5-7b it is observed that diffusivity of CO_2 in oil is highly underestimated. This is owed to the bigger bead sizes in CG models leading to a less degree of freedom for the movement of the molecules. An observation was made that at the temperature of 293.15 K, CO_2 diffusivity varied with a factor of 400 for type K6 and K9 oil as compared to the atomistic simulation values. For the temperature of 313.15 K, oil viscosity varied with a factor of 100 for type K6 and K9 oil as compared to the atomistic simulation values. Although the statistics are not sufficient, these correlations could be used to predict CO_2 diffusivity for different chain lengths of Krytox^{TM} oil at the same operating conditions of temperature and pressure.

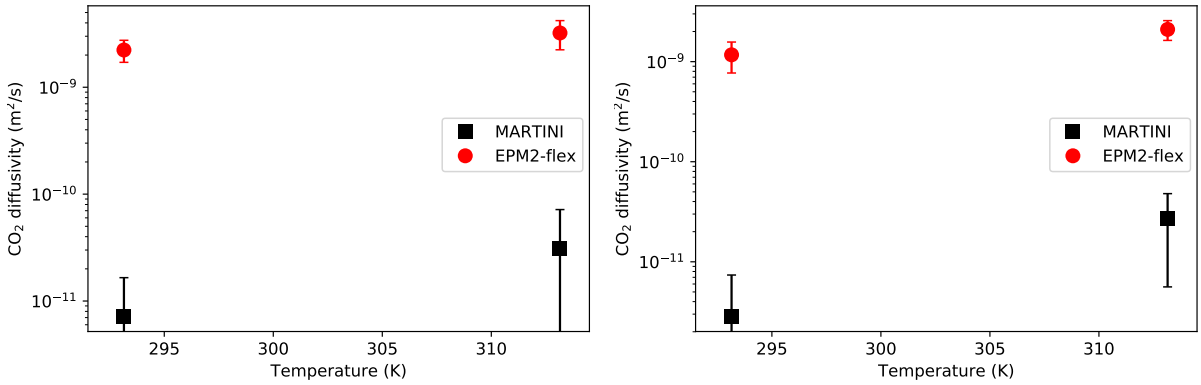

Figure 5-7: Comparison between the simulated CO_2 diffusivity in Krytox^{TM} oil for CG simulations using the MARTINI force field and atomistic simulations (UFF for oil and EPM2-flex for CO_2) for varying temperature at 1 atm pressure: (a) Type K6 oil; (b) Type K9 oil.

Table 5-2: Comparison (MARTINI, atomistic UFF, experimental) of properties of type K6 and type K9 oil at 1 atm pressure.

Oil type	Property	Model	Temperature (K)	
			293.15	**313.15**
K6	Density	MARTINI	2047 ± 26	2038 ± 20
		UFF	1762 ± 31	1724 ± 31
		Experiment	1852 [11]	1814 [11]
	Viscosity	MARTINI	453.9 ± 593.9	118.5 ± 62.7
		UFF	11.3 ± 6.7	5.4 ± 1.6
		Experiment	25.0 ± 0.1 [58]	14.1 ± 1.4 [11]
	CO_2 diffusivity	MARTINI	$7.13 \pm 9.41 \times 10^{-12}$	$3.12 \pm 4.05 \times 10^{-11}$
		UFF	$2.23 \pm 0.52 \times 10^{-9}$	$3.22 \pm 0.98 \times 10^{-9}$
K9	Density	MARTINI	2036 ± 9	2021 ± 15
		UFF	1795 ± 8	1755 ± 21
		Experiment	1865 [49]	1826 [49]
	Viscosity	MARTINI	1366 ± 456.1	239.8 ± 126.5
		UFF	47.6 ± 42.7	20.3 ± 11.1
		Experiment	62.8 ± 1.3 [49]	26.1 ± 0.5 [49]
	CO_2 diffusivity	MARTINI	$2.83 \pm 4.55 \times 10^{-12}$	$2.68 \pm 2.12 \times 10^{-11}$
		UFF	$1.17 \pm 0.40 \times 10^{-9}$	$2.10 \pm 0.47 \times 10^{-9}$

Units: Density ($kg\,m^{-3}$), Viscosity (cP), CO_2 diffusivity ($m^2\,s^{-1}$).
Mean values are reported with uncertainty calculated at 95% confidence interval.
Uncertainty data for experimental density is not available for all grades of oil and is thus not reported.

The radius of gyration and end to end distance was computed for CG simulations and were compared to the values from atomistic simulations using UFF. The mean values with uncertainty calculated at 95% confidence interval are reported in table 5-3. The higher values of radius of gyration and end to end distance for type K6 oil using MARTINI as compared to the UFF is attributed to the large size of bead. The lower value of end to end distance for type K9 oil using MARTINI as compared to the UFF is because MARTINI uses the position of the centre of mass of the bead for calculation.

Table 5-3: Geometric details obtained from simulations for type K6 and K9 oil at 313.15 K temperature and at 1 atm pressure.

Oil type	**Radius of gyration (Å)**		**End to end distance (Å)**	
	MARTINI	**UFF**	**MARTINI**	**UFF**
K6	6.52 ± 0.12	5.81 ± 0.54	16.02 ± 0.63	14.21 ± 4.71
K9	7.83 ± 0.21	7.84 ± 1.68	18.93 ± 1.01	21.03 ± 11.71

Mean values are reported with uncertainty calculated at 95% confidence interval.

Chapter 6

Solubility calculations for CO_2 in Krytox GPL 101

In section 1-2, reasons for the use of Krytox^{TM} oil as solvent for solubility of CO_2 have been cited. Usually, MC simulations are preferred for solubility calculations for their accuracy. In this project, prediction of Henry's constant was carried out using alchemical free energy calculations using MD simulations in LAMMPS. Experimental solubility data and thus data for Henry's constant is available for Krytox GPL 101 from the works by Dr H. Bazyar carried out at P&E laboratory, TU Delft. Thus calculations for the free energy of solvation were performed for solubility of CO_2 in Krytox GPL 101 by atomistic MD simulations. Type K6 oil (refer table 3-1) was considered for simulation purpose. UFF was considered for type K6 oil and EPM2-flex force field for CO_2 molecule. The chapter is divided into three parts. Section 6-1 covers the theoretical background and calculation methodology. The simulations details and discussion of results is carried out in sections 6-2 and 6-3 respectively.

6-1 Methodology of free energy calculations for computing Henry's constant

For solubility of a gas in a solvent, at equilibrium, the chemical potential of solute in the gas phase is equal to that in the liquid phase and is given by equation 6-1. The term on the left represents the chemical potential of solute in the gas phase and the term on right represents the chemical potential of solute in the liquid phase.

$$G_{\mathrm{s}}^{\mathrm{ig}}\left[T, p_{\mathrm{ref}}\right] + RT \ln\left(\frac{f_{\mathrm{s}}}{p_{\mathrm{ref}}}\right) = G_{\mathrm{s}}^{\circ}[T, p] + RT \ln\left(x_{\mathrm{s}}\gamma_{\mathrm{s}}^{\mathrm{H}}\right) \tag{6-1}$$

where:

G_s^{ig} = Gibbs energy of solute as an ideal gas
R = Universal gas constant
T = Temperature
f_s = Fugacity of solute
p_{ref} = Reference pressure = 0.1 MPa
G_s° = Gibbs free energy of solute in solvent at infinite dilution
x_s = Mole fraction of solute dissolved in the solvent
γ_s^H = Activity coefficient compatible with Henry's law

At infinite dilution, which is also the case for the solubility of CO_2 in Krytox^{TM} oil, the value of activity coefficient compatible with Henry's law i.e. γ_s^H is unity. By definition, Henry's constant (K_H) is given by equation 6-2. A point to note here is that for the system in consideration pressure (p) is equal to saturation pressure (p^{sat}) and thus Henry's constant is only a function of temperature.

$$K_H[T,p] = \lim_{x_s \to 0} \left(\frac{f_s}{x_s} \right) \tag{6-2}$$

By combining equations 6-1 and 6-2, equation 6-3 is obtained for free energy of solvation (ΔG_{sol}°).

$$RT \ln \left(\frac{K_H[T,p]}{p_{ref}} \right) = G_s^{\circ}[T,p] - G_s^{ig}[T,p_{ref}] = \Delta G_{sol}^{\circ}[T,p] \tag{6-3}$$

Free energy of solvation can be interpreted as the amount of energy change when a solute molecule is transferred from a gas phase (no interactions) to a solvent in liquid phase [32]. At a molecular level, the free energy of solvation can be interpreted in two parts:

- The energy required to create space for a solute molecule in the solvent.
- The energy change of the system when the solute interacts with the solvent molecule.

Part 1 is explicitly dependent on the property of solvent and is calculated analytically using equation 6-4 [32] where G_{SS} is the intrinsic value of Gibbs energy of solvent and V_W is the molar specific volume of solvent.

$$G_{SS} = RT \ln \left(\frac{RT}{p_{ref} V_W} \right) \tag{6-4}$$

Part 2 is related to the calculation of energy related to interaction and is carried out using the MD simulation method known as alchemical free energy (difference) calculations. As the word alchemy suggests, the process of free energy difference calculation is not physical. Figure 6-1 depicts the procedure for calculation of free energy difference for interaction. In the sub-figure on the left, the solute molecule completely interacts with the solvent molecules. In transition (A), the electric charges for solute-solvent interactions are turned off. In transition (B), the van der Waals forces are turned off (both electrostatic and van der Waals can be turned off simultaneously as well). The total energy change (including energy from part 1) of the system

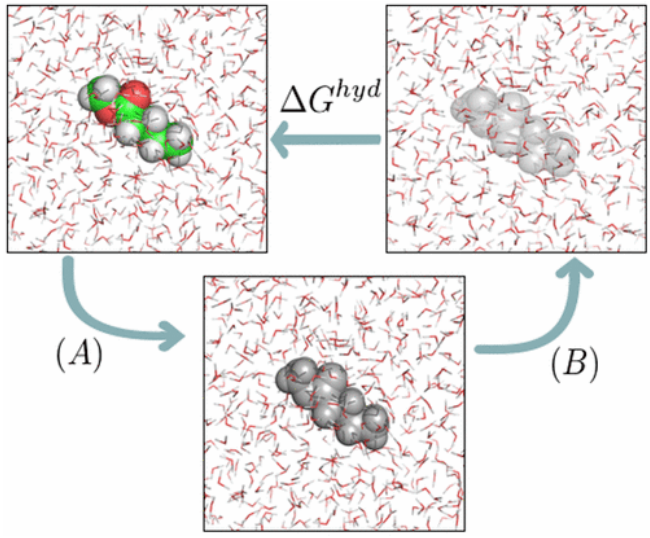

Figure 6-1: Steps for alchemical free energy of solvation (hydration) calculation. For representation, the solute molecule is shown large and the solvent molecules small. In transition (A), electrostatic interactions are turned off. In transition (B), van der Waals interactions are turned off. The total energy change is the free energy of interaction [31].

is the free energy of solvation. The solvent molecules interact among themselves throughout the entire process.

For the system of interest with one CO_2 molecule dissolved in type K6 oil, only van der Waals forces are responsible for the interaction with the implementation of the UFF model (refer chapter 3 for details). The van der Waals forces for solute-solvent interaction for free energy calculations are computed using LJ soft-core potential given by equation 6-5. λ is the interaction parameter where $\lambda = 1$ represents full interaction and $\lambda = 0$ represents no interaction. The value of λ was varied from 0 to 1 (and vice-versa) for the calculation of interaction energy. Values for exponent n and coefficient α_{LJ} were chosen as 1 and 0.5 respectively [31].

$$\mathcal{U}_{\mathrm{LJ}} = \lambda^n 4\varepsilon \left(\frac{1}{\left[\alpha_{\mathrm{LJ}}(1-\lambda)^2 + \left(\frac{r}{\sigma}\right)^6\right]^2} - \frac{1}{\alpha_{\mathrm{LJ}}(1-\lambda)^2 + \left(\frac{r}{\sigma}\right)^6} \right) \tag{6-5}$$

Free energy difference calculation can be performed using methods such as free-energy perturbation (FEP), finite-difference thermodynamic integration (FDTI) or Bennet's acceptance ratio method (BAR) [31]. For this project, FEP and FDTI methods were used in LAMMPS. Because of the non-linear path followed by free energy, the value of interaction parameter λ is varied in small steps from 0 to 1 (and vice-versa). In both the methods λ is perturbed from its existing value for computation of free energy difference. A point to note here is that free energy is path-independent, but this nonphysical method still yields the free energy change following a path in discrete steps. The details of the methods and their implementation in LAMMPS for the system of interest is described below.

6-1-1 Free-energy perturbation (FEP) method

Stepwise alchemical transformation using the FEP method is based on equation 6-6. For ensemble-averaged free energy difference ($\Delta_0^1 G$) calculation for CO_2 in type K6 oil, λ was varied from 0 to 1 (and vice-versa) in steps of 0.05. For every value of λ, a perturbation of +0.05 (on the existing value of λ) was enforced to calculate the free energy difference. Thus in 20 steps the entire domain from no interaction to full interaction was covered.

$$\Delta_0^1 G = \sum_{i=0}^{n-1} \Delta_{\lambda_i}^{\lambda_{i+1}} G = -k_B T \sum_{i=0}^{n-1} \ln \left\langle \exp\left(-\frac{\mathcal{U}(\lambda_{i+1}) - \mathcal{U}(\lambda_i)}{k_B T} \right) \right\rangle_{\lambda_i} \tag{6-6}$$

The same procedure was also followed for variation of λ from 1 to 0 with a perturbation of -0.05. By following the reverse procedure similar energy profile should be obtained. This was done to ensure that at each value of λ, the system was well equilibrated. Also, the values of total free energy difference obtained by both transitions should be the same (with opposite sign). In literature, it has been observed that the FEP method is accurate for small steps in λ, but with a lower sampling frequency, the exponential term leads to unstable free energy estimates and large biases because of tails of distribution that are not well sampled. This means that the phase space overlap is low and the configurations sampled from one energy state are likely improbable in the other state [31][70]. This was also observed for solubility of CO_2 in type K6 oil where the energy profiles obtained for transition $0 \rightarrow 1$ and $1 \rightarrow 0$ were not exactly similar.

6-1-2 Finite-difference thermodynamic integration (FDTI) method

Stepwise alchemical transformation using FDTI method is calculated using equation 6-7. It is based on an evaluation of the numerical derivative of the free energy by a perturbation method using a very small perturbation (δ). In this case as well λ was varied from 0 to 1 (and vice-versa) in steps of 0.05 with perturbation $\delta = +0.002$. At $\lambda = 1$, the perturbation leads to a perturbed value of $\lambda = 1.002$. Although nonphysical, this is required to cover the entire domain of λ from 0 to 1. Simpson's 1/3 rule was used to fix the weights of the numerical quadrature (w_i) [42]. Thus in 21 steps the entire domain from no interaction to full interaction was covered.

$$\Delta_0^1 G = \int_{\lambda=0}^{\lambda=1} \left\langle \frac{\partial \mathcal{U}(\lambda)}{\partial \lambda} \right\rangle_\lambda \mathrm{d}\lambda \approx \sum_{i=0}^{n-1} w_i \left\langle \frac{\mathcal{U}(\lambda_i + \delta) - \mathcal{U}(\lambda_i)}{\delta} \right\rangle_{\lambda_i} \tag{6-7}$$

The same procedure was also followed for variation of λ from 1 to 0 with perturbation of -0.002. Following this path, the last value of λ to which perturbation was provided was 0.002, resulting in a perturbed value of 0. This was done because negative values of λ do not exist. The method is more efficient than FEP as there is no bias in the method [70].

6-2 Simulation details and scheme

Experimental values of Henry's constant are available at temperatures 293.15 K and 323.15 K. Thus, free energy MD simulations were performed for these temperatures. The pressure

was taken as 1 atm. UFF parameters for Krytox^{TM} oil and EPM2-flex force field parameters for CO_2 as specified in tables 2-1 and 2-5 respectively were used. The simulation preparation method was the same as mentioned in section 3-1. The simulation steps followed are listed below:

- For each value of λ, energy minimization was performed using conjugate gradient method [14] for 1000 steps.
- In NPT ensemble, the system was equilibrated for 3 ns after which perturbed energy difference data (also in exponential form as required for FEP method) was sampled for 1 ns using *compute fep* command in LAMMPS.

The data was utilized for calculation of free energy of solvation and hence Henry's constant at different temperatures using equation 6-3.

6-3 Simulation results and experimental validation

Henry's constant was calculated at temperatures 293.15 K and 323.15 K using FEP, FDTI methods for transition of interaction parameter λ both from $0 \rightarrow 1$ and $1 \rightarrow 0$. Solvent Gibbs energy G_{SS} was calculated using equation 6-4 with reference pressure $p_{ref} = 0.1$ MPa and specific volume V_W calculated based on density obtained from MD simulation (refer table 4-1) with molecular weight of type K6 oil as 1134 $g\,mol^{-1}$. The results for calculation of Henry's constant and its comparison to experimental values is shown in tables 6-1 and 6-2. It is seen that at both 293.15 K and 323.15 K, Henry's constant is over-predicted by about 30% as compared to experimental values.

Table 6-1: Simulated and experimental value of Henry's constant at 293.15 K temperature.

Method	λ transition	ΔG_{MD} ($kJ\,mol^{-1}$)	ΔG°_{sol} ($kJ\,mol^{-1}$)	K_H (bar)	Exp K_H (bar)
FEP	$1 \rightarrow 0$	1.200	7.651	23.12	17.6
	$0 \rightarrow 1$	-1.529	7.323	20.21	
FDTI	$1 \rightarrow 0$	1.278	7.574	22.40	
	$0 \rightarrow 1$	-0.829	8.023	26.94	

$G_{SS} = 8.852\ kJ\,mol^{-1}$.
ΔG_{MD} is the free energy obtained from alchemical free energy calculation in MD simulation.
For λ transition $1 \rightarrow 0$, $\Delta G^{\circ}_{sol} = G_{SS}$ - ΔG_{MD}.
For λ transition $0 \rightarrow 1$, $\Delta G^{\circ}_{sol} = G_{SS}$ + ΔG_{MD}.

Figures 6-2 and 6-3 show variation of perturbed free energy for transition in interaction parameter λ using both FEP and FDTI methods. The FEP plots (figure 6-2) for transition of λ from $1 \rightarrow 0$ and $0 \rightarrow 1$ show some difference in the energy profile at lower λ values. This is also evident from the alchemical free energy transformation (ΔG_{MD}) values in table 6-2. The energy profiles could be improved by including more intermediate λ values [31]. On the other end energy profiles for FDTI plots (figure 6-3) are a better replicate of each other for λ transition from $1 \rightarrow 0$ and $0 \rightarrow 1$.

Table 6-2: Simulated and experimental value Henry's constant at 323.15 K temperature.

Method	λ transition	ΔG_{MD} (kJ mol^{-1})	ΔG°_{sol} (kJ mol^{-1})	K_H (bar)	Exp K_H (bar)
FEP	$1 \rightarrow 0$	0.541	9.420	33.38	26.35
	$0 \rightarrow 1$	-0.805	9.156	30.25	
FDTI	$1 \rightarrow 0$	0.539	9.422	33.40	
	$0 \rightarrow 1$	-0.448	9.513	34.55	

$G_{SS} = 9.961$ kJ mol^{-1}.
ΔG_{MD} is the free energy obtained from alchemical free energy calculation in MD simulation.
For λ transition $1 \rightarrow 0$, $\Delta G^{\circ}_{sol} = G_{SS}$ - ΔG_{MD}.
For λ transition $0 \rightarrow 1$, $\Delta G^{\circ}_{sol} = G_{SS}$ + ΔG_{MD}.

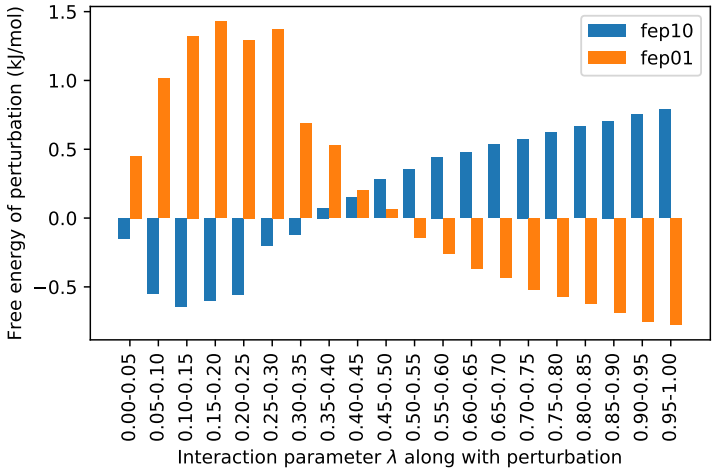

Figure 6-2: Free energy of perturbation using FEP method at 323.15 K temperature.

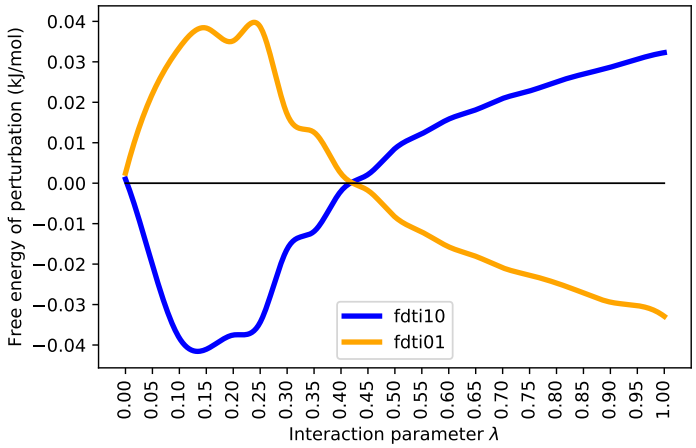

Figure 6-3: Free energy of perturbation using FDTI method at 323.15 K temperature.

Chapter 7

Summary and conclusions

Transport properties namely the viscosity of Krytox^{TM} oil and diffusivity of CO_2 in the oil were predicted using MD simulations. Also, the solubility of CO_2 in Krytox GPL 101 was computed using alchemical free energy calculations.

In section 2-3-5, preliminary simulations were performed using different force fields to determine a suitable force field for studying Krytox^{TM} oil. Density values of Krytox GPL 102 were predicted using UFF, OPLS-AA and CVFF force fields and were found to be within 5% of the experimental value. Because of the long-range electrostatic potential, the simulated viscosity value of Krytox GPL 102 did not converge using OPLS-AA and CVFF force fields for EMD simulations. UFF does not explicitly account for the electric charges leading to faster convergence of oil viscosity. Thus, UFF was selected as the force field of choice for the study of properties of Krytox^{TM} oil.

In chapter 3, simulation methodology and details for computing transport properties were described. In chapter 4, simulation results for the study of viscosity of Krytox^{TM} oil and CO_2 diffusivity in the oil for a range of temperature, pressure and polymer chain length values were presented. All the simulations were performed by the EMD method in LAMMPS using the OCTP tool for transport properties prediction. Krytox GPL 101 and 102 were studied in detail for their availability of experimental data. Transport properties were also studied for other chain lengths to predict a trend for variation of properties for varying chain length.

Oil density was under-predicted by about 5% compared to the experimental values using UFF. The difference in experimental and simulated viscosity value was high (simulated viscosity was under-predicted) at low temperatures and the difference decreased towards high temperatures. Variation in viscosity followed Arrhenius relation (equation 4-3) and variation in CO_2 diffusivity followed a linear relation as predicted by Stokes-Einstein equation (equation 4-4) for variation in temperature of the system. At high pressures, the variation in CO_2 diffusivity in the oil was minimal owing to the closed packing of the oil molecules. For an increase in the chain length of the oil molecule, a quadratic increase in the oil viscosity was observed. A steeper decrease in the CO_2 diffusivity was observed for a variation of oil chain

length from 4 to 8 monomers per molecule as compared to an increase in the chain length from 8 to 13 monomers per molecule. Since polymeric oil is a mixture of molecules with differing chain lengths, systems equivalent to Krytox GPL 101 and 102 with different types of oil molecules (based on the number of monomers in a chain) in a simulation box were studied. It was observed that these systems predicted similar properties when compared to homogeneous systems with a single molecule type. Structural properties including the radius of gyration, end to end length and RDFs of atoms of CO_2 molecule concerning the atoms of the oil molecule were studied. Stretching was observed for a shorter chain length oil molecule attributed to overcoming of energy barrier by hydrodynamic forces whereas coiling was observed for a longer polymer chain owing to entropy effects.

To improve on the simulation time and thus the computational efficiency of the long chain Krytox^{TM} oil molecule, in chapter 5, CG simulations for Krytox GPL 101 and 102 with the number of monomers = 6, 9 in a chain respectively were performed using the MARTINI force field in GROMACS. The density was over-predicted by about 10%. Large variation in oil viscosity and CO_2 diffusivity was observed by CG simulations using the MARTINI force field. Nonetheless, some trends could be predicted for transport properties for variation of polymer chain length. These could be related to the experimental data.

In addition to the prediction of transport properties, in chapter 6, Henry's constant was predicted for solubility of CO_2 in Krytox^{TM} oil via alchemical free energy calculations by atomistic MD simulations. Henry's constant was over-predicted by about 30% as compared to the experimental value.

To conclude, atomistic MD simulations provided insight into the transport and thermodynamic properties of Krytox^{TM} oil - CO_2 mixture. It was possible to study properties for a wide range of operating conditions after an initial validation of simulated density and viscosity data for Krytox GPL 101 and 102 with the available experimental data. Also, for varying chain length of polymeric oil, the behaviour of the properties variation was studied which would have been difficult to study with experiments alone. MD simulations made it possible to compute the diffusivity of gas in a solvent directly from the trajectory data of molecules which in the case of experiments would have required obtaining it from the solubility data. Many trends in properties were observed for variation in temperature, pressure and chain length which could prove to be useful for product development and process design for application of Krytox^{TM} oil to SLM. In addition, an attempt was made towards performing computationally efficient CG simulations using the MARTINI force field, the power of which could be exploited further.

Chapter 8

Recommendations

EMD simulations were performed for their ability to predict multiple transport properties from a single simulation. For atomistic simulations, it was observed that because of the electrostatic interactions, OPLA-AA and CVFF force fields were not practical for EMD simulations for their slow convergence of viscosity owing to the highly viscous nature of Krytox^{TM} oil. In such cases, it is recommended to perform NEMD simulations to test the possibility to use other prospective force fields. In addition, to validate the diffusivity of CO_2 in Krytox^{TM} oil obtained from MD simulations, further experiments are required to be performed.

Regarding CG simulations, it is recommended to perform extensive simulations using the MARTINI force field to obtain an exact correlation for the variation of properties to the experimental values. Also, potentials for the energy of torsion should be parameterized, as in this study, only the potentials for bond stretching and bond bending were considered. For accurate measurement of solubility of CO_2 in Krytox^{TM} oil, MC simulations should be carried out to validate the use of UFF for computing Henry's constant.

Appendix A

Derivation of parameters for C-C-C angle for the UFF force field

For the unavailability of force field parameters for C-C-C bond bending in the literature by Jiang et al. [24], literature for the UFF force field parameters by Rappe et al. [41] was referred for obtaining the parameters.

In equation A-1, I, J, K represent the first, second and third atoms of the angle respectively. r_{IJ} and r_{IJ} are the bond distances both of which are equal to 1.514 Å. Equilibrium angle $\theta_0 = 109.47°$ for C-C-C.

In equation A-2, β is the undetermined parameter.

In equation A-3, Z_{I} and Z_{K} are the effective charges for I and K atom both of which are equal to 1.912. Value of force constant for angle bending $\mathrm{K_{IJK}}$ was found equal to 236.528 $\mathrm{kcal\,mol^{-1}}$.

$$r_{\mathrm{IK}}^2 = r_{\mathrm{IJ}}^2 + r_{\mathrm{JK}}^2 - 2r_{\mathrm{IJ}}r_{\mathrm{JK}}\cos\theta_0 \tag{A-1}$$

$$\beta = \frac{664.12}{r_{\mathrm{IJ}}r_{\mathrm{JK}}} \tag{A-2}$$

$$\mathrm{K_{IJK}} = \beta\frac{Z_{\mathrm{I}}Z_{\mathrm{K}}}{r_{\mathrm{IK}}^5}r_{\mathrm{IJ}}r_{\mathrm{JK}}\left[3r_{\mathrm{IJ}}r_{\mathrm{JK}}\left(1-\cos^2\theta_0\right) - r_{\mathrm{IK}}^2\cos\theta_0\right] \tag{A-3}$$

Appendix B

LAMMPS implementation of various force field models

This section lists the parameters for various force field models as implemented in LAMMPS for the selection of force field in section 2-3. Various LAMMPS specific bonded and non-bonded potential types as used by different force field models are listed below.

Bond stretching was defined by *harmonic* style potential as specified by equation B-1.

$$\mathcal{U}_{\mathrm{R}} = K\left(r - r_0\right)^2 \tag{B-1}$$

Bond bending was defined by *harmonic* style potential as specified by equation B-2.

$$\mathcal{U}_{\theta} = K\left(\theta - \theta_0\right)^2 \tag{B-2}$$

Bond torsion can be specified defined by *fourier* style (equation B-3), *charmm* style (equation B-4), *OPLS* style (equation B-5) potential or *harmonic* (equation B-6) style.

$$\mathcal{U}_{\phi} = \sum_{i=1,m} K_i\left[1 + \cos\left(n_i\phi - d_i\right)\right] \tag{B-3}$$

$$\mathcal{U}_{\phi} = K[1 + \cos(n\phi - d)] \tag{B-4}$$

$$\begin{aligned}\mathcal{U}_{\phi} =& \frac{1}{2}K_1(1 + \cos\phi) + \frac{1}{2}K_2(1 - \cos 2\phi) + \\ & \frac{1}{2}K_3(1 + \cos 3\phi) + \frac{1}{2}K_4(1 - \cos 4\phi)\end{aligned} \tag{B-5}$$

$$\mathcal{U}_{\phi} = K\left(1 + d\cos n\phi\right) \tag{B-6}$$

Van der Waals forces were defined by Lennard-Jones potential as specified by equation B-7.

$$\mathcal{U}_{\mathrm{LJ}} = 4\varepsilon \left[\left(\frac{\sigma}{r} \right)^{12} - \left(\frac{\sigma}{r} \right)^{6} \right] \tag{B-7}$$

Potential for electrostatic interaction takes the form specified by equation B-8.

$$\mathcal{U}_{\mathrm{el}} = \frac{1}{4\pi\varepsilon_0} \frac{q_i q_j}{r} \tag{B-8}$$

The potentials for bond stretching, bond bending, Van der Waals and electrostatic interaction have a unique style of representation. There are various options for bond torsion, the choice for which is indicated separately for the individual force field.

B-1 OPLS-AA

OPLS-AA force field parameters as adapted by Black et al. [25] and implemented in LAMMPS are listed in table B-1. Bond torsion was defined by *fourier* style as specified by equation B-3. Shifted LJ potential with a cut-off distance of 12 Å was used. Standard arithmetic mixing rules, $\varepsilon_{ij} = (\varepsilon_i\ \varepsilon_j)^{1/2}$, $\sigma_{ij} = (\sigma_i + \sigma_j)/2$, were used for deriving LJ parameters for atoms of different types. For electrostatic interactions cut-off distance was specified as 12 Å with long-range correction using pppm solver [39] with 10^{-6} units as the accuracy of relative error in forces. LJ and electrostatic potentials were considered for the atoms separated by atleast two atoms. 1-4 atom interaction potential (non-bonded) was scaled by a factor of 0.5.

B-2 GAFF

GAFF [43] parameters as implemented in LAMMPS are listed in table B-2. Bond torsion was defined by *charmm* (equation B-4) and *OPLS* (equation B-5) styles and is indicated in table B-2c. A cut-off distance of 12 Å was used for LJ potential with a correction for tail interactions [14]. Standard arithmetic mixing rules, $\varepsilon_{ij} = (\varepsilon_i\ \varepsilon_j)^{1/2}$, $\sigma_{ij} = (\sigma_i + \sigma_j)/2$, were used for deriving LJ parameters for atoms of different types. For electrostatic interactions cut-off distance was specified as 9 Å with long-range correction using pppm solver [39] with 10^{-6} units as the accuracy of relative error in forces. The charges were derived using RESP [44] and are specific only to $C_8F_{18}O_4$ molecule. LJ and electrostatic potentials were considered for the atoms separated by atleast two atoms. 1-4 atom interaction for LJ potential was scaled by a factor of 0.833 and for electrostatic potential by a factor of 0.5.

B-3 CVFF

CVFF [23] parameters as implemented in LAMMPS are listed in table B-3. Bond torsion was defined by *harmonic* style as specified by equation B-6. A cut-off distance of 9 Å was used for LJ potential with a correction for tail interactions [14]. Standard geometric mixing rules, $\varepsilon_{ij} = (\varepsilon_i\ \varepsilon_j)^{1/2}$, $\sigma_{ij} = (\sigma_i\ \sigma_j)^{1/2}$, were used for deriving LJ parameters for atoms of different

Table B-1: OPLS-AA force field parameters.

(a) Bond parameters.

Bond type	K (kcal mol^{-1} Å^{-2})	r_0 (Å)
C-C	268.000	1.529
C-O	320.000	1.360
C-F	367.000	1.332

(b) Angle parameters.

Angle type	K (kcal mol^{-1})	θ_0 (°)
C-C-O	50.000	107.800
C-C-F	50.000	109.500
C-O-C	60.000	121.400
F-C-O	50.000	110.700
F-C-F	77.000	109.100
C-C-C	58.350	112.700

(c) Dihedral parameters.

Dih type	**m**	K_1	n_1	d_1	K_2	n_2	d_2	K_3	n_3	d_3	K_4	n_4	d_4	K_5	n_5	d_5
F-C-O-C	5	−2.91	0	90	0.00	1	0	0.00	2	-180	0.87	3	62	3.02	4	-97
O-C-O-C	5	−8.25	0	90	3.87	1	15	1.63	2	-144	1.79	3	66	3.73	4	-93
C-C-O-C	5	0.00	0	90	22.09	1	-14	0.00	2	-180	4.24	3	-93	−4.87	4	-265
O-C-C-F	5	0.00	0	90	0.00	1	0	0.00	2	-180	0.90	3	0	0.00	4	-180
O-C-C-O	5	2.48	0	90	0.00	1	0	−0.96	2	-180	−0.36	3	0	0.00	4	-180
O-C-C-C	5	1.91	0	90	0.00	1	0	−0.87	2	-193	0.87	3	33	0.00	4	-180
F-C-C-F	5	0.00	0	90	−1.25	1	0	0.00	2	0	0.13	3	0	0.00	4	0
C-C-C-F	5	0.00	0	90	0.15	1	0	0.00	2	0	0.20	3	0	0.00	4	0

Units: K_x (kcal mol^{-1}), where x = 1, 2, 3, 4, 5.

(d) Non-bonded parameters.

Atom type	ε (kcal mol^{-1})	σ (Å)	q (e)
C1	0.066	3.50	0.240
C2	0.066	3.50	0.440
C3	0.066	3.50	0.360
C4	0.066	3.50	0.320
F	0.053	2.95	−0.120
O	0.152	3.00	−0.400

C1: Carbon atom connected to 2 F and 2 C atoms.
C2: Carbon atom connected to 2 F, 1 O and 1 C atoms.
C3: Carbon atom connected to 3 F and 1 C atoms.
C4: Carbon atom connected to 1 F, 1 O and 2 C atoms.

Table B-2: GAFF force field parameters.

(a) Bond parameters.

Bond type	K **(kcal mol^{-1} Å^{-2})**	r_0 **(Å)**
C-C	303.100	1.535
C-O	301.500	1.439
C-F	363.800	1.344

(b) Angle parameters.

Angle type	K **(kcal mol^{-1})**	θ_0 **(°)**
C-C-O	67.800	108.420
C-C-F	66.200	109.410
C-O-C	62.100	113.410
F-C-O	71.500	63.045
F-C-F	71.300	107.160

(c) Dihedral parameters.

Dihedral type	K	n	d	**wt. factor**	**Remarks**
F-C-C-F	1.200	1	180	0	CHARMM
C-C-C-F	0.156	3	0	0	CHARMM
	K_1	K_2	K_3	K_4	
C-C-O-C	0	0.20	0.766	0	OPLS
O-C-C-O	0	2.35	0.288	0	OPLS

Units: K_x (kcal mol^{-1}), where x = 1, 2, 3, 4, none.

(d) Non-bonded parameters.

Atom type	ε **(kcal mol^{-1})**	σ **(Å)**	q **(e)**
C1	0.109	3.40	0.6146
C2	0.109	3.40	0.2313
F1	0.061	3.12	−0.1514
F2	0.061	3.12	−0.0772
O1	0.170	3.00	−0.2253
O2	0.170	3.00	−0.1658

C1: Carbon atom connected to 3 F atoms.
C2: Other carbon atoms.
F1: Fluorine atom connected to C1 atom.
F2: Fluorine atom connected to C2 atom.
O1: Oxygen atom connected to C1 and C2 atoms.
O2: Oxygen atom connected to C2 atoms.

types. For electrostatic interactions cut-off distance was specified as 12 Å with long-range correction using pppm solver [39] with 10^{-6} units as the accuracy of relative error in forces. LJ and electrostatic potentials were considered for the atoms separated by atleast two atoms. 1-4 atom interaction potential (non-bonded) was scaled by a factor of 0.5.

Table B-3: CVFF force field parameters.

(a) Bond parameters.

Bond type	K **(kcal mol^{-1} Å^{-2})**	r_0 **(Å)**
C-C	322.932	1.526
C-O	273.383	1.425
C-F	496.332	1.363

(b) Angle parameters.

Angle type	K **(kcal mol^{-1})**	θ_0 **(°)**
C-C-O	70.047	109.500
C-C-F	99.066	107.800
C-O-C	60.040	109.500
F-C-O	95.064	107.800
F-C-F	95.064	107.800
C-C-C	46.631	110.500

(c) Dihedral parameters.

Dihedral type	K **(kcal mol^{-1})**	d	n
X-C-O-X	0.390	1	3
X-C-C-X	1.423	1	3

X: Any atom type.

(d) Non-bonded parameters.

Atom type	ε **(kcal mol^{-1})**	σ **(Å)**	q **(e)**
C1	0.160	3.47	0.3539
C2	0.160	3.47	0.4529
C3	0.160	3.47	0.5338
C4	0.160	3.47	0.2750
F	0.069	3.08	−0.1779
O	0.228	2.86	−0.1941

C1: Carbon atom connected to 2 F and 2 C atoms.
C2: Carbon atom connected to 2 F, 1 O and 1 C atoms.
C3: Carbon atom connected to 3 F and 1 C atoms.
C4: Carbon atom connected to 1 F, 1 O and 2 C atoms.

Appendix C

GROMACS implementation of OPLS-AA force field

This section lists the parameters for the OPLS-AA force field by Jorgensen et al. [26] as implemented in GROMACS for atomistic simulation of Krytox^{TM} oil in section 5-2-1.

Bond stretching was defined by *harmonic* style potential as specified by equation C-1.

$$\mathcal{U}_{\mathrm{R}} = \frac{1}{2}K\left(r - r_0\right)^2 \tag{C-1}$$

Bond bending was defined by *harmonic* style potential as specified by equation C-2.

$$\mathcal{U}_{\theta} = \frac{1}{2}K\left(\theta - \theta_0\right)^2 \tag{C-2}$$

Bond torsion was defined by *fourier* style potential as specified by equation C-3.

$$\begin{aligned}\mathcal{U}_{\phi} =& \frac{1}{2}C_1(1+\cos\phi) + \frac{1}{2}C_2(1-\cos 2\phi) + \frac{1}{2}C_3(1+\cos 3\phi) + \\ & \frac{1}{2}C_4(1-\cos 4\phi) + \frac{1}{2}C_5(1+\cos 5\phi)\end{aligned} \tag{C-3}$$

Van der Waals forces were defined by Lennard-Jones potential as specified by equation C-4.

$$\mathcal{U}_{\mathrm{LJ}} = 4\varepsilon\left[\left(\frac{\sigma}{r}\right)^{12} - \left(\frac{\sigma}{r}\right)^{6}\right] \tag{C-4}$$

Potential for electrostatic interaction take the form specified by equation C-5.

$$\mathcal{U}_{\mathrm{el}} = \frac{1}{4\pi\varepsilon_0}\frac{q_i q_j}{r} \tag{C-5}$$

Shifted LJ potential with a cut-off distance of 12 Å was used. Standard arithmetic mixing rules, $\varepsilon_{ij} = (\varepsilon_i\ \varepsilon_j)^{1/2}$, $\sigma_{ij} = (\sigma_i + \sigma_j)/2$, were used for deriving LJ parameters for atoms

of different types. For electrostatic interactions cut-off distance was specified as 12 Å with long-range correction using Fast smooth Particle-Mesh Ewald (SPME) with 10^{-4} units as the accuracy of relative error in forces. LJ and electrostatic potentials were considered for the atoms separated by atleast two atoms. 1-4 atom interaction potential (non-bonded) was scaled by a factor of 0.5.

Table C-1: OPLS-AA force field parameters.

(a) Bond parameters.

Bond type	K **(kJ mol^{-1} nm^{-2})**	r_0 **(nm)**
C-C	224262.4	0.1529
C-O	267776.0	0.1410
C-F	307105.6	0.1332

(b) Angle parameters.

Angle type	K **(kJ mol^{-1})**	θ_0 **(°)**
C-C-O	418.400	109.5
C-C-F	418.400	109.5
C-O-C	502.080	109.5
F-C-O	774.877	111.5
F-C-F	644.336	109.1
C-C-C	488.273	112.7

(c) Dihedral parameters.

Dihedral type	C_1	C_2	C_3	C_4	C_5
F-C-O-C	0.000	0.000	3.180	0.000	0.000
O-C-O-C	-2.180	-8.443	8.351	0.000	0.000
C-C-O-C	2.720	-1.046	2.803	0.000	0.000
O-C-C-F	0.000	0.000	1.958	0.000	0.000
O-C-C-O	-2.301	0.000	0.000	0.000	0.000
O-C-C-C	7.159	-2.092	2.774	0.000	0.000
F-C-C-F	-10.460	0.000	1.046	0.000	0.000
C-C-C-F	1.255	0.000	1.674	0.000	0.000

Units: C_x (kJ mol^{-1}), where x = 1, 2, 3, 4, 5.

(d) Non-bonded parameters.

Atom type	ε **(kJ mol^{-1})**	σ **(nm)**	q **(e)**
C1	0.2761	0.350	0.240
C2	0.2761	0.350	0.440
C3	0.2761	0.350	0.360
C4	0.2761	0.350	0.320
F	0.2218	0.295	−0.120
O	0.5858	0.300	−0.400

C1: Carbon atom connected to 2 F and 2 C atoms.
C2: Carbon atom connected to 2 F, 1 O and 1 C atoms.
C3: Carbon atom connected to 3 F and 1 C atoms.
C4: Carbon atom connected to 1 F, 1 O and 2 C atoms.

Bibliography

[1] D. M. D'Alessandro, B. Smit, and J. R. Long, "Carbon dioxide capture: Prospects for new materials," *Angewandte Chemie - International Edition*, vol. 49, no. 35, pp. 6058–6082, 2010.

[2] M. Ramdin, T. Z. Olasagasti, T. J. Vlugt, and T. W. De Loos, "High pressure solubility of CO2 in non-fluorinated phosphonium-based ionic liquids," *Journal of Supercritical Fluids*, vol. 82, pp. 41–49, 2013.

[3] N. M. Kocherginsky, Q. Yang, and L. Seelam, "Recent advances in supported liquid membrane technology," *Separation and Purification Technology*, vol. 53, no. 2, pp. 171–177, 2007.

[4] P. Cserjési, N. Nemestóthy, and K. Bélafi-Bakó, "Gas separation properties of supported liquid membranes prepared with unconventional ionic liquids," *Journal of Membrane Science*, vol. 349, no. 1-2, pp. 6–11, 2010.

[5] T. Hoefling, D. Stofesky, M. Reid, E. Beckman, and R. M. Enick, "The incorporation of a fluorinated ether functionality into a polymer or surfactant to enhance C02-solubility," *The Journal of Supercritical Fluids*, vol. 5, no. 4, pp. 237–241, 1992.

[6] M. J. Muldoon, S. N. Aki, J. L. Anderson, J. K. Dixon, and J. F. Brennecke, "Improving carbon dioxide solubility in ionic liquids," *Journal of Physical Chemistry B*, vol. 111, no. 30, pp. 9001–9009, 2007.

[7] M. B. Shiflett and A. Yokozeki, "Solubilities and diffusivities of carbon dioxide in ionic liquids: [bmim][PF6] and [bmim][BF4]," *Industrial and Engineering Chemistry Research*, vol. 44, no. 12, pp. 4453–4464, 2005.

[8] J. L. Anthony, E. J. Maginn, and J. F. Brennecke, "Solubilities and thermodynamic properties of gases in the ionic liquid 1-n-butyl-3-methylimidazolium hexafluorophosphate," *Journal of Physical Chemistry B*, vol. 106, no. 29, pp. 7315–7320, 2002.

[9] H. G. Joglekar, I. Rahman, and B. D. Kulkarni, "The path ahead for ionic liquids," *Chemical Engineering and Technology*, vol. 30, no. 7, pp. 819–828, 2007.

[10] Chemours, "Krytox performance lubricants product overview," 2020.

[11] Dupont, "Dupont krytox performace lubricants," 2020.

[12] "Avogadro: an open-source molecular builder and visualization tool. version 1.2.0."

[13] H. O. Baled, D. Tapriyal, B. D. Morreale, Y. Soong, I. Gamwo, V. Krukonis, B. A. Bamgbade, Y. Wu, M. A. McHugh, W. A. Burgess, and R. M. Enick, "Exploratory Characterization of a Perfluoropolyether Oil as a Possible Viscosity Standard at Deepwater Production Conditions of 533K and 241MPa," *International Journal of Thermophysics*, vol. 34, no. 10, pp. 1845–1864, 2013.

[14] M. P. Allen and D. J. Tildesley, *Computer simulation of liquids*. Oxford university press, 2017.

[15] M. Valiev, E. J. Bylaska, N. Govind, K. Kowalski, T. P. Straatsma, H. J. Van Dam, D. Wang, J. Nieplocha, E. Apra, T. L. Windus, and W. A. De Jong, "NWChem: A comprehensive and scalable open-source solution for large scale molecular simulations," *Computer Physics Communications*, vol. 181, no. 9, pp. 1477–1489, 2010.

[16] P. Raveendran and S. L. Wallen, "Exploring CO2-philicity: Effects of stepwise fluorination," *Journal of Physical Chemistry B*, vol. 107, no. 6, pp. 1473–1477, 2003.

[17] P. K. Parhi, "Supported liquid membrane principle and its practices: A short review," *Journal of Chemistry*, vol. 2013, 2013.

[18] J. D. Seader, E. J. Henley, and D. K. Roper, *Separation process principles*, vol. 25. Wiley New York, 1998.

[19] H. C. Li, C. McCabe, S. T. Cui, P. T. Cummings, and H. D. Cochran, "Development of a force field for molecular simulation of the phase equilibria of perfluoromethylpropyl ether," *Molecular Physics*, vol. 100, no. 2, pp. 265–272, 2002.

[20] C. McCabe, D. Bedrov, O. Borodin, G. D. Smith, and P. T. Cummings, "Transport Properties of Perfluoroalkanes Using Molecular Dynamics Simulation: Comparison of United- and Explicit-Atom Models," *Industrial and Engineering Chemistry Research*, vol. 42, no. 26, pp. 6956–6961, 2003.

[21] S. T. Cui, J. I. Siepmann, H. D. Cochran, and P. T. Cummings, "Intermolecular potentials and vapor-liquid phase equilibria of perfluorinated alkanes," *Fluid Phase Equilibria*, vol. 146, no. 1-2, pp. 51–61, 1998.

[22] O. Borodin, G. D. Smith, and D. Bedrov, "A quantum chemistry based force field for perfluoroalkanes and poly(tetrafluoroethylene)," *Journal of Physical Chemistry B*, vol. 106, no. 38, pp. 9912–9922, 2002.

[23] A. Koike, "Molecular dynamics study of tribological behavior of confined branched and linear perfluoropolyethers," *Journal of Physical Chemistry B*, vol. 103, no. 22, pp. 4578–4589, 1999.

[24] B. Jiang, D. J. Keffer, and B. J. Edwards, "Estimation and analysis of the rheological properties of a perfluoropolyether through molecular dynamics simulation," *Journal of Fluorine Chemistry*, vol. 127, no. 6, pp. 787–795, 2006.

[25] J. E. Black, G. M. Silva, C. Klein, C. R. Iacovella, P. Morgado, L. F. Martins, E. J. Filipe, and C. McCabe, "Perfluoropolyethers: Development of an All-Atom Force Field for Molecular Simulations and Validation with New Experimental Vapor Pressures and Liquid Densities," *Journal of Physical Chemistry B*, vol. 121, no. 27, pp. 6588–6600, 2017.

[26] W. L. Jorgensen, D. S. Maxwell, and J. Tirado-Rives, "Development and testing of the OPLS all-atom force field on conformational energetics and properties of organic liquids," *Journal of the American Chemical Society*, vol. 118, no. 45, pp. 11225–11236, 1996.

[27] S. Plimpton, "LAMMPS Molecular Dynamics Simulator."

[28] S. H. Jamali, L. Wolff, T. M. Becker, M. De Groen, M. Ramdin, R. Hartkamp, A. Bardow, T. J. Vlugt, and O. A. Moultos, "OCTP: A Tool for On-the-Fly Calculation of Transport Properties of Fluids with the Order- n Algorithm in LAMMPS," *Journal of Chemical Information and Modeling*, vol. 59, no. 4, pp. 1290–1294, 2019.

[29] P. C. T. Souza, R. Alessandri, J. Barnoud, S. Thallmair, I. Faustino, F. Grünewald, I. Patmanidis, H. Abdizadeh, B. M. H. Bruininks, T. A. Wassenaar, P. C. Kroon, J. Melcr, V. Nieto, V. Corradi, H. M. Khan, J. Domański, M. Javanainen, H. Martinez-seara, N. Reuter, R. B. Best, I. Vattulainen, L. Monticelli, X. Periole, D. P. Tieleman, A. H. D. Vries, and S. J. Marrink, "Martini 3: a general purpose force field for coarse-grained molecular dynamics," *Nature Methods*, vol. 18, no. 4, pp. 382–388, 2021.

[30] Lindahl, Abraham, Hess, and van der Spoel, "Gromacs 2021.2 manual," May 2021.

[31] G. Duarte Ramos Matos, D. Y. Kyu, H. H. Loeffler, J. D. Chodera, M. R. Shirts, and D. L. Mobley, "Approaches for Calculating Solvation Free Energies and Enthalpies Demonstrated with an Update of the FreeSolv Database," *Journal of Chemical and Engineering Data*, vol. 62, no. 5, pp. 1559–1569, 2017.

[32] V. Majer, J. Sedlbauer, and G. Bergin, "Henry's law constant and related coefficients for aqueous hydrocarbons, CO2 and H2S over a wide range of temperature and pressure," *Fluid Phase Equilibria*, vol. 272, no. 1-2, pp. 65–74, 2008.

[33] D. Frenkel and B. Smit, *Understanding molecular simulation: from algorithms to applications*, vol. 1. Elsevier, 2001.

[34] S. I. Sandler, *An introduction to applied statistical thermodynamics*. John Wiley & Sons, 2010.

[35] D. Dubbeldam, D. C. Ford, D. E. Ellis, and R. Q. Snurr, "A new perspective on the order-n algorithm for computing correlation functions," *Molecular Simulation*, vol. 35, no. 12-13, pp. 1084–1097, 2009.

[36] R. Taylor and R. Krishna, *Multicomponent mass transfer*, vol. 2. John Wiley & Sons, 1993.

[37] A. T. Celebi, S. H. Jamali, A. Bardow, T. J. Vlugt, and O. A. Moultos, "Finite-size effects of diffusion coefficients computed from molecular dynamics: a review of what we have learned so far," *Molecular Simulation*, vol. 0, no. 0, pp. 1–15, 2020.

[38] M. Mondello and G. S. Grest, "Viscosity calculations of n-alkanes by equilibrium molecular dynamics," *Journal of Chemical Physics*, vol. 106, no. 22, pp. 9327–9336, 1997.

[39] R. W. Hockney and J. W. Eastwood, *Computer simulation using particles*. crc Press, 1988.

[40] C. I. Bayly, K. M. Merz, D. M. Ferguson, W. D. Cornell, T. Fox, J. W. Caldwell, P. A. Kollman, P. Cieplak, I. R. Gould, and D. C. Spellmeyer, "A Second Generation Force Field for the Simulation of Proteins, Nucleic Acids, and Organic Molecules," *Journal of the American Chemical Society*, vol. 117, no. 19, pp. 5179–5197, 1995.

[41] A. K. Rappé, C. J. Casewit, K. S. Colwell, W. A. Goddard, and W. M. Skiff, "UFF, a Full Periodic Table Force Field for Molecular Mechanics and Molecular Dynamics Simulations," *Journal of the American Chemical Society*, vol. 114, no. 25, pp. 10024–10035, 1992.

[42] S. C. Chapra, *Applied numerical methods: with MATLAB for engineers and scientists*. McGraw-Hill, 2008.

[43] J. Wang, R. M. Wolf, J. W. Caldwell, P. A. Kollman, and D. A. Case, "Development and testing of a general Amber force field," *Journal of Computational Chemistry*, vol. 25, no. 9, pp. 1157–1174, 2004.

[44] C. I. Bayly, P. Cieplak, W. D. Cornell, and P. A. Kollman, "A well-behaved electrostatic potential based method using charge restraints for deriving atomic charges: The RESP model," *Journal of Physical Chemistry*, vol. 97, no. 40, pp. 10269–10280, 1993.

[45] E. Vanquelef, S. Simon, G. Marquant, E. Garcia, G. Klimerak, J. C. Delepine, P. Cieplak, and F.-Y. Dupradeau, "R.E.D. Server: a web service for deriving RESP and ESP charges and building force field libraries for new molecules and molecular fragments," *Nucleic Acids Research*, vol. 39, pp. W511–W517, 05 2011.

[46] F.-Y. Dupradeau, A. Pigache, T. Zaffran, C. Savineau, R. Lelong, N. Grivel, D. Lelong, W. Rosanski, and P. Cieplak, "The r.e.d. tools: advances in resp and esp charge derivation and force field library building," *Physical Chemistry Chemical Physics*, vol. 12, no. 28, p. 7821, 2010.

[47] "Gaussian: Expanding the limits of computational chemistry."

[48] P. Dauber-Osguthorpe, V. A. Roberts, D. J. Osguthorpe, J. Wolff, M. Genest, and A. T. Hagler, "Structure and energetics of ligand binding to proteins: Escherichia coli dihydrofolate reductase-trimethoprim, a drug-receptor system," *Proteins: Structure, Function, and Bioinformatics*, vol. 4, no. 1, pp. 31–47, 1988.

[49] S. K. Mylona, M. J. Assael, L. Karagiannidis, P. D. Jannakoudakis, and W. A. Wakeham, "Measurements of the viscosity of krytox GPL102 oil in the temperature range (282 to 364) K and up to 20 MPa," *Journal of Chemical and Engineering Data*, vol. 60, no. 12, pp. 3539–3544, 2015.

[50] H. Zhong, S. Lai, J. Wang, W. Qiu, H. D. Lüdemann, and L. Chen, "Molecular Dynamics Simulation of Transport and Structural Properties of CO2 Using Different Molecular Models," *Journal of Chemical and Engineering Data*, vol. 60, no. 8, pp. 2188–2196, 2015.

[51] H. G. Hanwell Marcus, Curtis Donald, Lonie David, Vandermeersch Tim, Eva Zurek, "Avogadro: an advanced semantic chemical editor, visualization, and analysis platform," *Journal of Cheminformatics*, vol. 4, 2012.

[52] J. M. M. L. Martinez, R. Andrade, E. G. Birgin, "Packmol: A Package for Building Initial Configurations for Molecular Dynamics Simulations," *Journal of computational chemistry*, vol. 30, no. 13, pp. 2157–2163, 2009.

[53] W. Humphrey, A. Dalke, and K. Schulten, "VMD – Visual Molecular Dynamics," *Journal of Molecular Graphics*, vol. 14, pp. 33–38, 1996.

[54] D. J. Evans and B. L. Holian, "The nose–hoover thermostat," *The Journal of chemical physics*, vol. 83, no. 8, pp. 4069–4074, 1985.

[55] J. Milzetti, D. Nayar, and N. F. A. van der Vegt, "Convergence of kirkwood buff integrals of ideal and nonideal aqueous solutions using molecular dynamics simulations," *The Journal of Physical Chemistry B*, vol. 122, no. 21, pp. 5515–5526, 2018. PMID: 29342355.

[56] P. Ganguly and N. F. A. V. D. Vegt, "Convergence of Sampling KirkwoodBuff Integrals of Aqueous Solutions with Molecular Dynamics Simulations," *Journal of Chemical Theory and Computation*, vol. 9, pp. 1347–1355, 2013.

[57] *Viscosity-Temperature Correlation for Liquids*, vol. Part A: Tribomaterials; Lubricants and Additives; Elastohydrodynamic Lubrication; Hydrodynamic Lubrication and Fluid Film Bearings; Rolling Element Bearings; Engine Tribology; Machine Components Tribology; Contact Mechanics of *International Joint Tribology Conference*, 10 2006.

[58] H. Bazyar, P. Lv, J. A. Wood, S. Porada, D. Lohse, and R. G. Lammertink, "Liquid-liquid displacement in slippery liquid-infused membranes (SLIMs)," *Soft Matter*, vol. 14, no. 10, pp. 1780–1788, 2018.

[59] F. V. Schmelzer JW, Zanotto ED, "Pressure dependence of viscosity," *Journal of Chemical Physics*, vol. 122, no. Feb 2005, 2005.

[60] S. I. Sandler, *An introduction to applied statistical thermodynamics*. Wiley, 2011.

[61] S. J. Marrink, H. J. Risselada, S. Yefimov, D. P. Tieleman, and A. H. De Vries, "The MARTINI force field: Coarse grained model for biomolecular simulations," *Journal of Physical Chemistry B*, vol. 111, no. 27, pp. 7812–7824, 2007.

[62] S. J. Marrink, A. H. D. Vries, and A. E. Mark, "Coarse grained model for semiquantitative lipid simulations," *The Journal of Physical Chemistry B*, vol. 108, no. 2, p. 750–760, 2004.

[63] J. Barnoud, "https://jbarnoud.github.io/cgbuilder/cgbuilder."

[64] S. Páll and B. Hess, "A flexible algorithm for calculating pair interactions on simd architectures," *Computer Physics Communications*, vol. 184, no. 12, pp. 2641–2650, 2013.

[65] L. Verlet, "Computer "experiments" on classical fluids. i. thermodynamical properties of lennard-jones molecules," *Phys. Rev.*, vol. 159, pp. 98–103, Jul 1967.

[66] G. Bussi, D. Donadio, and M. Parrinello, "Canonical sampling through velocity rescaling," *The Journal of Chemical Physics*, vol. 126, no. 1, p. 014101, 2007.

[67] M. Parrinello and A. Rahman, "Polymorphic transitions in single crystals: A new molecular dynamics method," *Journal of Applied Physics*, vol. 52, no. 12, p. 7182–7190, 1981.

[68] N. Kondratyuk, D. Lenev, and V. Pisarev, "Transport coefficients of model lubricants up to 400 MPa from molecular dynamics," *The Journal of Chemical Physics*, vol. 152, no. 19, p. 191104, 2020.

[69] G. Van Rossum and F. L. Drake Jr, *Python reference manual*. Centrum voor Wiskunde en Informatica Amsterdam, 1995.

[70] M. R. Shirts, V. S. Pande, M. R. Shirts, and V. S. Pande, "Comparison of efficiency and bias of free energies computed by exponential averaging , the Bennett acceptance ratio , and thermodynamic integration Comparison of efficiency and bias of free energies computed by exponential averaging , the Bennett acceptan," *The Journal of Chemical Physics*, vol. 122, 2005.

Nomenclature

Abbreviations

AA	All-atom
BAR	Bennet's acceptance ratio
CG	Coarse-grained
CVFF	Consistent valence force field
EMD	Equilibrium molecular dynamics
EPM2	Elementary physical model 2
FDTI	Finite-difference thermodynamic integration
FEP	Free-energy perturbation
GAFF	General Amber force field
LAMMPS	Large-scale Atomic/Molecular Massively Parallel Simulator
LJ	Lennard-Jones
MC	Monte Carlo
MD	Molecular dynamics
MSD	Mean-squared displacement
NEMD	Non-equilibrium molecular dynamics
NPT	Isothermal-isobaric ensemble
NVE	Microcanonical ensemble
NVT	Canonical ensemble
OCTP	On-the-fly computation of transport properties
OPLS-AA	Optimized potential for liquid simulations all-atom
RDF	Radial distribution function
SLM	Supported liquid membranes
TraPPE	Transferable potentials for phase equilibria
UFF	Universal force field
VMD	Visual MD

Physical constants

ε_0	Vacuum dielectric permittivity	$8.8542 \times 10^{-12}\,\mathrm{F\,m^{-1}}$
k_B	Boltzmann constant	$1.3806 \times 10^{-23}\,\mathrm{m^2\,kg\,s^{-2}\,K^{-1}}$
R	Universal gas constant	$8.3145\,\mathrm{J\,mol^{-1}\,K^{-1}}$

Variables

A	Dynamic variable
C	Concentration / Constant
D	Diffusivity
d	Integer
f	Force / Fugacity
$\mathbf{F}$	Force vector
$g(r)$	Correlation function
G	Gibb energy
K	Force constant
K_H	Henry's constant
L	Length
l	Characteristic length
N	Flux / Number of molecules/atoms
n	number of monomers
P	Permeability / Pressure tensor component
p	Pressure
q	Charge
r	Distance / radius of gyration
$\mathbf{r}$	Position vector
T	Temperature
t	Time
$\mathcal{U}$	Potential energy
$\mathbf{v}$	Velocity vector
V	Volume
v	Velocity
w	Weight factor of integration
x	Mole fraction
Z	Effective charge

Greek variables

α	Coefficient
α_p	Thermal expansion coefficient
Δ	Difference
δ	Perturbation
η	Dynamic viscosity
Γ	Thermodynamic factor
γ	Phase / Transport property / Activity coefficient

κ_T	Isothermal compressibility
Λ	Onsager coefficient
λ	Eigenvalue / Interaction parameter
ε	Lennard-Jones energy
ϕ	Dihedral angle
π	Pi
ρ	Density
σ	Lennard-Jones diameter
θ	Angle
ξ	Dimensionless number

Superscripts

∞	Finite-size correction
H	Henry's constant
ig	Ideal gas
o	Standard state of infinite dilution

Subscripts

0	Initial / Equilibrium
α	Component of stress tensor
β	Component of stress tensor
F	Feed side
i	Variable
j	Variable
k	Variable
l	Variable
m	Variable
n	Variable
P	Permeate side
p	Pressure
ϕ	Dihedral angle
θ	Angle
avg	Average
el	Electrostatic
eq	Equilibrium
I	Variable
J	Variable
K	Variable
LJ	Lennard-Jones
MD	Molecular dynamics
MS	Maxwell-Stefan
R	Bond

ref	Reference
S	Saturation
s	Solute
sol	Solvation
SS	Intrinsic value
tot	Total
vdW	van der Waals
W	Reference to specific molar volume

Others

$\langle\rangle$	Ensemble average